Rethinking the global secondary organic aerosol (SOA) budget: stronger production, faster removal, shorter lifetime

Hodzic A.[1], Kasibhatla P.S.[2], Jo D.S.[3], Cappa C.[4], Jimenez J.L.[5], Madronich S.[1], Park R.J.[3].

[1]*National Center for Atmospheric Research, Boulder, CO, USA*
[2]*Nicholas School of the Environment, Duke University, Durham, USA*
[3]*School of Earth and Environmental Science, Seoul National University, Republic of Korea*
[4]*University of California, Davis, USA*
[5]*University of Colorado, Boulder, USA*
Correspondence to A. Hodzic: ***alma@ucar.edu***
Key words*: secondary organic aerosol, dry and wet deposition, heterogeneous reactions, photolysis, wall-corrected yields*

Abstract: Recent laboratory studies suggest that secondary organic aerosol (SOA) formation rates are higher than assumed in current models. There is also evidence that SOA removal by dry and wet deposition occurs more efficiently than some current models suggest, and that photolysis and heterogeneous oxidation may be important (but currently ignored) SOA sinks. Here, we have updated the global GEOS-Chem model to include this new information on formation (i.e. wall-corrected yields and emissions of semi-volatile and intermediate volatility organic compounds) and on removal processes (photolysis and heterogeneous oxidation). We compare simulated SOA from various model configurations against ground, aircraft and satellite measurements to assess the extent to which these improved representations of SOA formation and removal processes are consistent with observed characteristics of the SOA distribution. The updated model presents a more dynamic picture of the lifecycle of atmospheric SOA, with production rates 3.9 times higher and sinks a factor of 3.6 more efficient than in the base model. In particular, the updated model predicts larger SOA concentrations in the boundary layer and lower concentrations in the upper troposphere, leading to better agreement with surface and aircraft measurements of organic aerosol compared to the base model. Our analysis thus suggests that the long-standing discrepancy in model predictions of the vertical SOA distribution can now be resolved, at least in part, by a stronger source and stronger sinks leading to a shorter lifetime. The predicted global SOA burden in the updated model is 0.88 Tg and the corresponding direct radiative forcing at top of the atmosphere is -0.33 W m^{-2}, which is comparable to recent model estimates constrained by observations. The updated model predicts a population-weighed global mean surface SOA concentration that is a factor of 2 higher than in the base model, suggesting the need for a reanalysis of the contribution of SOA to PM pollution-related human health effects. The potential importance of our estimates highlights the need for more extensive field and laboratory studies focused on characterizing organic aerosol removal mechanisms and rates.

1 Introduction

Secondary organic aerosol (SOA) is formed through complex photochemical gas and aqueous reactions involving a variety of biogenic and anthropogenic hydrocarbons, and accounts for a substantial fraction of the submicron aerosol mass [*Zhang et al.,* 2007]. Despite its importance from a climate and air quality perspective, there are significant uncertainties in our understanding of SOA. A recent intercomparison study of more than twenty state-of-the-art global aerosol models showed that estimates of the SOA annual production rate vary among models by an order of magnitude, from ~13 to 119 Tg yr^{-1}, and estimates of its lifetime range from 5 to 15 days [*Tsigaridis et al.,* 2014]. This wide spread in model results arises from a limited knowledge of underlying processes controlling both SOA formation and removal in the atmosphere.

SOA formation rates used in current large scale models are commonly based on yields derived from chamber experiments, which might be severely underpredicted (up to a factor of 4) due to loses of organic vapors onto chamber walls [*La et al.,* 2015; *Zhang et al.,* 2014; *Matsunaga and Ziemann,* 2010]. As a consequence, these models often significantly underpredict ambient SOA concentrations [e.g. *Heald et al.,* 2011; *Spracklen et al.,* 2011]. To compensate for these model underestimations in an effort to match surface organic aerosol (OA) and SOA measurements, models increasingly include unconstrained aging parameterizations in which more volatile organic constituents are converted to less volatile ones [e.g. *Jo et al.,* 2013; *Shrivastava et al.,* 2011; *Tsimpidi et al.,* 2010]. A detailed analysis by *Heald et al.* [2011] suggests however that an adjustment of this sort will lead to other biases in model performance. In their study, global model simulations that were adjusted to correctly reproduce surface concentrations of organic aerosols (OA) displayed unrealistic accumulation of OA in the upper troposphere. These studies suggest that in addition to SOA formation processes,

64 there is also a need to re-examine the representation of SOA removal processes in
65 chemistry-climate models.

66 Wet scavenging is typically the major direct loss (90%) of SOA in global models
67 [*Tsigaridis et al.,* 2014], with dry deposition representing a much smaller sink (<10%)
68 due to the small dry deposition velocities predicted for accumulation mode aerosols
69 [*Seinfeld and Pandis,* 2006; *Farmer et al.,* 2013]. SOA loss can also occur indirectly by
70 wet and dry removal of gas phase semi-volatile oxidized species, which act to suppress
71 the amount of condensable material available for SOA formation through gas-particle
72 partitioning. Global models typically treat the removal of these gas-phase oxidized
73 organic compounds (OVOCs) in an ad-hoc manner using constant Henry's law solubility
74 coefficients between 10^3 and 10^6 M atm^{-1} [*Knote et al.,* 2015 and references therein].
75 However, recent explicit modeling results [*Hodzic et al.*, 2014] show that Henry's law
76 solubility coefficients can vary significantly as a function of the volatility of OVOCs,
77 indicating the need for a reassessment of effective wet and dry removal lifetimes of
78 SOA.

79 In addition to wet and dry removal, there is increasing evidence of other potentially
80 important SOA loss mechanisms that are, to our knowledge, rarely implemented in
81 global model calculations. Laboratory studies suggest that photolytic processing of
82 organic gases and particles can remove tropospheric aerosols on timescales
83 comparable to those of wet deposition, although the chemical transformations involved
84 are not well understood [*Henry and Donahue,* 2012; *Epstein et al.,* 2014; *Wong et al.,*
85 *2014*]. Model estimates performed by *Hodzic et al.* [2015] indicate that SOA photolytic
86 frequencies equivalent to 0.04% of typical NO_2 photolysis frequencies can decrease
87 SOA tropospheric concentrations by 20-60%. Furthermore, organic compounds at or
88 near the surface of particles were also found to be sensitive to heterogeneous (surface)

oxidation by OH and O_3 [*Moise and Rudich,* 2002; *Molina et al.,* 2004; *Kroll et al.,* 2009; *George and Abbatt,* 2010; *Ortega et al.,* 2015]. An attempt to include this process in a global model by oxidizing SOA with OH with an effective gas-phase-equivalent rate constant of 10^{-12} cm^3 $molecule^{-1}s^{-1}$ and assuming that only 5% of reacted molecules is lost, suggested a 25% loss of SOA in the upper troposphere and 15% elsewhere [*Heald et al.,* 2011]. The implications of O_3 oxidation on the large-scale SOA distribution have not yet been estimated using 3D models. Given the potential effect of these processes on SOA lifecycle, there is a need to estimate the relative efficiency of SOA removal by these competing pathways in a common modeling framework.

In this study, we focus on re-assessing the global SOA distribution, budget and radiative forcing in light of new insights into SOA production and loss processes in the atmosphere derived from recent laboratory measurements and theoretical calculations. We perform a series of model sensitivity simulations using the GEOS-Chem global model to evaluate the importance of the wall-corrected SOA yields, the additional emissions of semi-volatile and intermediate volatility organic species, as well as the effect of additional removal pathways discussed above on the SOA spatial distribution and budget. We then compare simulated SOA from these sensitivity runs against a suite of surface and free tropospheric measurements to investigate whether the updated treatment of sources and sinks leads to a more realistic simulation of observed spatial SOA patterns.

2 Modeling approach

In this study, we use the GEOS-Chem global chemical transport model [*Bey et al.,* 2001] at a horizontal resolution of 2° × 2.5° with 47 vertical hybrid pressure-sigma levels up to 0.01 hPa to conduct simulations of aerosol-oxidant chemistry for 2005-2008 with a spin-up of 1 year (2004). The model (http://acmg.seas.harvard.edu/geos/index.html) uses assimilated meteorological data from the Goddard Earth Observing System (GEOS-5) of the NASA Global Modeling and Assimilation Office (GMAO). The standard version of GEOS-Chem includes a comprehensive description of tropospheric NO_X-hydrocarbon-O_3 gas-phase chemistry, as well as the treatment of major aerosol components including sulfate, nitrate, ammonium, black carbon, and primary (POA) and secondary organic aerosols. Anthropogenic VOC emissions are taken from the REanalysis of the TROpospheric chemical composition (RETRO) inventory, whereas POA emissions are from *Bond et al.* [2007]. Biomass burning emissions for all species are based on the Global Fire Emission Database version 3 (GFEDv3) inventory. Biogenic emissions are calculated online using the MEGAN v2.1 model [*Guenther et al.,* 2012]. Here, we use v.9.1.2 of the model with an added extension for SOA that incorporates a Volatility Basis Set (VBS) approach as described in *Jo et al.* [2013]. This base SOA model configuration is described in Section 2.1. We have implemented specific updates to account for wall-corrected SOA yields, SOA formation from additional long chain n-alkanes, solubility of organic vapors, and heterogeneous and photolytic loss of SOA, as described in Sections 2.2 and 2.3.

2.1 Base SOA model configuration

The base version of GEOS-Chem uses the volatility basis set approach (hereafter referred as VBS_REF) to simulate SOA as previously described in *Jo et al.* [2013]. In this approach, oxygenated semi-volatile organic compounds formed by the gas-phase

134 reaction of hydrocarbon species such as isoprene, monoterpenes, sesquiterpenes, and
135 aromatic compounds, with OH, O_3, and NO_3 are allocated to 4 volatility bins with
136 saturation concentrations (C*) of 1, 10, 100 to 1000 μg m^{-3} at 300K. Two additional
137 volatility bins 0.01 and 0.1 μg m^{-3} are used to represent SOA formed from aged
138 anthropogenic precursors by further reactions of OVOCs with OH. Partitioning between
139 gas and particle phase in each bin in each model grid cell is calculated based on the
140 total OA concentration and temperature in the grid cell. The temperature dependence of
141 the partitioning coefficient is calculated based on an assumed value for the enthalpy of
142 vaporization of 112 kJ mol^{-1} at C* = 0.01 μg m^{-3} with a decrease of 6 kJ mol^{-1} for each
143 increase in order of magnitude of C* [*Robinson et al.,* 2007]. Chemical aging of
144 anthropogenic oxidation intermediates with OH is considered with a rate constant of
145 $4x10^{-11}$ cm^3 $molecule^{-1}$ s^{-1} and leads to a reduction of the vapor pressure of the products
146 by one order of magnitude. There was no mass increase (oxygen gain) upon aging
147 reaction. Biogenic precursors are not artificially aged. It should be noted that we do not
148 support in any case the *ad hoc* aging of oxidation products, but since this is a common
149 modeling practice [e.g. *Tsimpidi et al.,* 2010; *Jo et al.,* 2013] we use it in this study as a
150 basis for comparisons with our updated model described below.

151 **2.2 Updated parameterization of SOA formation**

152 We have updated the SOA formation mechanism to use a modified set of VBS product
153 yields (called hereafter VBS_NEW) for which the influence of vapor wall-losses on the
154 SOA yields in chamber studies have been, at least approximately, accounted for.
155 Specifically, synthetic SOA yield curves (i.e. the amount of SOA formed versus the
156 amount of VOC reacted) were generated using the Statistical Oxidation Model (SOM)
157 based on previously-derived fits to chamber data [*Cappa and Wilson*, 2012]. The SOM
158 accounts for the influence of multi-generational chemistry, including both

functionalization and fragmentation. The SOM parameterizations are unique to precursor species and NO_X conditions. The SOM parameters are determined by fitting laboratory chamber data, specifically the time-evolution of the SOA formed during oxidation of a given VOC. All experiments considered were performed in the Caltech chambers and results from the fits are summarized in *Zhang et al.* [2014]. The SOM framework can account for the influence of losses of semi- and low-volatility vapors to the chamber walls on SOA formation using the *Matsunaga and Ziemann* [2010] methodology, and as described by *Zhang et al.* [2014]. The appropriate value to use for the vapor wall-loss rate coefficient (k_{wall}) remains a point of discussion, but can vary between chambers due to differences in chamber size and operation. Here, a value of $k_{wall} = 10^{-4}$ s^{-1} was assumed. This is likely a conservative (i.e. low) estimate as *Zhang et al.* [2014] derived a slightly larger value (2.5×10^{-4} s^{-1}) and *Matsunaga and Ziemann* [2010] a substantially larger value ($\sim 10^{-3}$ s^{-1}), albeit in the latter case for a different chamber. Here, this conservative estimate is used so as to provide an initial assessment of the influence of vapor wall losses, the effects of which may actually be larger than simulated here if the appropriate k_{wall} is larger than 10^{-4} s^{-1} [*Cappa et al.,* 2016]. For isoprene specifically, which contains two double bonds and can form products that react as fast, if not faster than, isoprene itself, especially under low NO_X conditions [*Paulot et al.,* 2009; *Surratt et al.,* 2010; *St. Clair et al.,* 2015], an isoprene-specific version of SOM was also used to fit the chamber observations. Parameterizations resulting from both the original and isoprene-specific SOM formulations have been described and compared in the Supplemental Material (Figure S1 and Table S2). The primary results in this work are based on the isoprene-specific formulation.

Results from SOM simulations are used to determine parameters for use in the volatility basis set (VBS) model framework. Specifically, after determining a set of SOM

parameters for each precursor with vapor wall losses accounted for, a set of simulations were run for each precursor VOC with: constant [OH] = $2x10^6$ molecules cm^{-3}; run time = 36h; absorbing seed concentration = 10 μg m^{-3}; precursor [VOC] = 1 ppt. The SOM product species from these simulations were then binned by their saturation concentration into logarithmically spaced bins (e.g. logC* ranging from -2 to 3, see Table 1) according to their gas + particle phase concentrations at the end of the simulation, and normalized by the total precursor concentration to determine mass yields as a function of volatility. Thus, the long-time (36 h) VBS mass yields can be calculated as:

$$a_{VBS,x} = \frac{\sum_{\log C^*_{SOM,i} \geq x-0.5}^{\log C^*_{SOM,i} < x+0.5} C_{SOM,i}}{\Delta[HC]}$$

where $a_{VBS,x}$ indicates the mass yield in VBS bin defined as $\log C^*_{VBS} = x$, $C_{SOM,i}$ is the gas + particle mass concentration of a given SOM species *i* after 36 h of reaction and $C^*_{SOM,i}$ is the saturation concentration of that species, and Δ[HC] is the reacted amount of a given parent hydrocarbon. All species with log $C^*_{SOM,i}$ < -2.5 were added to the $\log C^*_{VBS}$ = -2 bin. This produces a VBS for each compound for use in the global simulations that effectively accounts for the influence of vapor wall losses and, to first order, for the long-time influence of multi-generational chemistry. This new set of parameters used in the VBS_NEW model is summarized in Table 1 for low- and high-NO_X SOA production from monoterpenes, isoprene, sesquiterpenes, benzene, toluene and xylene. Similar to *Jo et al.* [2013], we use the low-NO_X yield values for biogenic species since most of the biogenic emissions occur over low-NO_X forested regions and since the coarse model resolution cannot resolve high-NO_X conditions. This is also consistent with the previous global model study by *Pye et al.* [2010], which reported that more than 90% of biogenic hydrocarbon reactions proceed through the low-NO_X pathway. For anthropogenic

206 species, we perform a linear interpolation between low- and high-NO_X values for
207 anthropogenic species based on the relative ratio of HO_2 and NO at the location and
208 time of VOC oxidation [*Lane et al.,* 2008]. The range of volatilities was extended to 6
209 bins, from 0.01 to 1000 μg m^{-3} at 300K for all species. The enthalpy of vaporization was
210 updated to the experimentally derived values starting at 151 kJ mol^{-1} at C* = 0.01 μg m^{-3}
211 and decreasing by 11 kJ mol^{-1} for each increase in order of magnitude of C* [*Epstein et*
212 *al.*, 2010].

213 The artificial aging of anthropogenic oxidation products is no longer considered in this
214 updated model. However, it is important to note that the SOM accounts for multi-
215 generational oxidation implicitly, including both functionalization and fragmentation
216 reaction pathways, while the VBS type models do not. Therefore, when VBS_NEW yield
217 distributions are determined from the corrected yield curves (or even when determined
218 from the uncorrected yield curves) the influence of multi-generational oxidation (aging)
219 on the observed SOA formation is, to some extent, captured in the derived VBS yield
220 parameters even though the VBS fits assume the OVOC product species are unreactive.
221 In contrast, the aging reactions included in the base-case VBS_REF model above
222 (Section 2.1., REF run) are added *ad hoc* on top of the original parameterization, which
223 can lead to substantial overestimates of the SOA formation [*Jathar et al.,* 2016; *Dzepina*
224 *et al.,* 2011; *Lane et al.,* 2008]. The addition of this *ad hoc* aging results in higher yields
225 and the formation of less volatile organic species from anthropogenic precursors in the
226 default VBS_REF model [*Jo et al.,* 2013] compared to the updated VBS_NEW as
227 demonstrated for Toluene in Figure S2.

228 It is worth noting that the chamber data set used here to determine the modified
229 VBS_NEW parameters is not identical to that used to determine the base-case
230 VBS_REF parameters. However, *Jathar et al.* [2016] have demonstrated that there are

231 relatively small differences between the amounts of SOA simulated using the new data
232 set versus using a traditional set of parameters when a 2-product approach is used,
233 which suggests that this data set difference should have minimal influence on the
234 VBS_NEW simulations here. The method used here to determine the modified
235 VBS_NEW parameters (fitting of a vapor wall-loss adjusted synthetic data set) is an
236 extension of the approach of *Cappa et al.* [2016], where they fitted a set of 2-product
237 yields [*Odum et al.,* 1996] to the synthetic (wall loss corrected) model runs, and where
238 they found that the 2-product model fits were not sufficiently robust due to the limited
239 number of fit parameters. The use of a 6-product parameterization here was found to
240 allow for reasonable fits to the synthetic yield curves. The difference between
241 uncorrected yields and wall-corrected yields (1.1 to 4.1 times) is shown in the
242 supplementary material (Figure S3).

243 In this study, we also include SOA formation from the oxidation of long-chain n-alkanes
244 (C>12) emitted from fossil-fuel, biofuel, and biomass burning sources [e.g. *Robinson et*
245 *al.,* 2007; *Gentner et al.,* 2012]. These semi-volatile (SVOC) and intermediate (IVOC)
246 volatility organic compounds are typically not included in traditional emission inventories.
247 This gap arises from the fact that SVOCs are lost rapidly by evaporation upon dilution
248 are thus not accounted for as primary emissions, and as well as a typical lack of
249 characterization and quantification IVOC compounds in emission studies. Based on the
250 analysis by *Jathar et al.* [2014, their Table 1], we set SVOC mass emissions as 60% of
251 POA emissions and IVOC emissions as 20% of NMVOC emissions (not including SVOC
252 emissions) in each grid cell. We consider both anthropogenic and biomass burning
253 emissions of S/IVOC. The emitted S/IVOCs can undergo oxidation with OH in the model,
254 and produce OVOCs that can partition to form SOA. Table 1 shows the volatility
255 distribution of produced OVOCs (and thus the corresponding SOA yields) that were

derived from the GECKO-A model (Generator of Explicit Chemistry and Kinetics of Organics in the Atmosphere, [*Aumont et al.,* 2005]) for low and high NO_X conditions considering a mixture of n-alkane species shown in Table 3 [*Lee-Taylor et al.,* 2011]. GECKO-A explicitly accounts for the multi-generational oxidation of OVOCs, including both functionalization and fragmentation reaction pathways, and thus the multi-generational aging of OVOCs from S/IVOCs is implicitly built into the VBS_NEW parameterization provided in Table 1. For GECKO-A, VBS yield distributions were derived in a similar manner as was done for determining distributions from SOM for the other SOA precursors (discussed above), assuming background OA concentrations of 10 μg m^{-3} and simulation conditions similar to *Hodzic et al.* [2014]. For computational efficiency, OVOC formation from SVOC was mapped to that of IVOCs by increasing the yields by 20%, which corresponds to the ratio in mass yields between SVOC and IVOCs as calculated from GECKO-A.

Global annual mean (2005-2008) emissions of I/SVOC were estimated to be about 54 Tg yr^{-1} (split evenly between biomass-burning and fossil/biofuels source categories) based on the corresponding emissions of POA (36.8 Tg yr^{-1} biomass burning; 19.7 Tg yr^{-1} fossil- and bio-fuels) and of NMVOC (23.7 Tg yr^{-1} biomass burning; 74.9 Tg yr^{-1} fossil- and biofuels). The resulting production of secondary organic gases with the updated VBS_NEW parameterization is 13 Tg yr^{-1} for biomass burning sources, and an additional 13 Tg yr^{-1} for fossil- and bio-fuels sources. Our S/IVOC emission estimates (53.6 Tg yr^{-1}) are on the low side of the values used in previous studies. For example, Shrivastava et al. [2015] assumed that SIVOC emissions were 6.5 times those of POA from biomass burning and fossil fuels, which lead to 234 Tg yr^{-1} of S/IVOC gases. *Jathar et al.* [2011] assumed that IVOC emissions (84.6 Tg yr^{-1}) were 1.5 times those of POA, which lead to the formation of 27.3 Tg yr^{-1} of SOA (close to our estimates of total SOA from S/IVOC).

They also modeled POA emissions (56.4 Tg yr^{-1}) as SVOC gases, assuming that POA was semi-volatile following the volatility distribution of *Robinson et al.* [2007], and that SVOC oxidation formed 22.5 Tg yr^{-1} of SOA, and that the rest equilibrated to form POA.

2.3 Updated parameterization of SOA removal

2.3.1 Dry and wet deposition

In GEOS-Chem, soluble gases and aerosols are removed by both convective and grid-scale precipitation as described by *Liu et al.* [2001]. Similar to other global model studies, a fixed value of the effective Henry's law solubility coefficient (H^{eff}) of 10^5 M atm^{-1} was used in the base model configuration for all intermediate OVOC gas-phase species that can partition to form SOA [*Jo et al.,* 2013]. Aerosol wet scavenging efficiency is set to 80% as in the standard GEOS-Chem model [*Chung and Seinfeld*, 2002]. We modified the model to account for the volatility dependence of the Henry's law water solubility coefficients for these species based on *Hodzic et al.* [2014]. H^{eff} values used are summarized in Table 2. For traditional anthropogenic precursors, we use H^{eff} typical of oxidation products of n-alkanes while for biogenic precursors we use H^{eff} values typical of oxidation products of monoterpenes. For oxidation products of IVOCs, we use H^{eff} of 10^3 M atm^{-1}.

Dry deposition of organic gases and particles is represented by the standard resistance approach [*Wesely,* 1989; *Seinfeld and Pandis,* 2006], which depends on meteorological conditions through atmospheric and laminar resistances, surface type through the surface resistance, and gravitational settling velocity for particles. The surface resistance describes partitioning of gases into plants and wet surfaces. For particles the surface resistance is set to zero as particles are assumed to stick to the surface. We note however that the GEOS-Chem configuration used by *Jo et al.* [2013] did not include dry deposition of organic vapors. In this study, we include dry deposition of organic vapors

using the same volatility-dependent Henry's law coefficients as in the wet deposition parameterization (Table 2).

2.3.2 Photolytic removal of particle phase organics

We also include the SOA loss by photolysis as a first order reaction following the parameterization proposed by *Hodzic et al.* [2015]. We assume that absorption of each photon by an SOA molecule leads to the irreversible loss of one carbon atom (as the lowest possible limit) from the molecule with a quantum yield of QY. With this assumption, the loss rate of SOA can be written as:

$$d[SOA]/dt = -J_{SOA} \times [SOA] \quad (1)$$

where

$$J_{SOA} = AF \times MAC \times QY \times m_c \quad (2)$$

In these equations, J_{SOA} is the first order photolysis rate coefficient for SOA integrated over the 280-400nm wavelength range, [SOA] is the SOA mass concentration (g m^{-3}), *AF* is the total actinic flux over 280-400nm (photons m^{-2} s^{-1}), *MAC* is the SOA mass absorption coefficient (m^2 g^{-1}), *QY* is the quantum yield (atoms of C/photon), and m_c is mass of a C atom (g). J_{SOA} can be rewritten in terms of the NO_2 photolysis rate coefficient (J_{NO2}) as:

$$J_{SOA} = 2\times10^{22} \times J_{NO2} \times MAC \times QY \times m_c \quad (3)$$

where $2x10^{22}$ (in units of photons m^{-2}) is the value of [AF/J_{NO2}] estimated by the photolysis model TUV (http://cprm.acom.ucar.edu/Models/TUV/Interactive_TUV/) [*Madronich et al.,* 1993] for overhead sun conditions at 1 km altitude over 280-400nm. This value varies by only ±5% over a range of solar zenith angles (0 to 90°), altitudes (1 to 10km), overhead ozone column (250 to 400 Dobson Units), and summer and winter conditions.

Similar to *Hodzic et al.* [2015] here, we use *MAC* = 0.1 m^2g^{-1} and *QY* = 0.01 (or 1%) as a representative value for ambient SOA aerosols. The resulting value for J_{SOA} is 0.04% of J_{NO2} ($J_{SOA} = 4 \times 10^{-4} \times J_{NO2}$) which is more than an order of magnitude lower than the photolysis loss coefficients reported by *Henry and Donahue* [2012] who estimated the photolytic loss of SOA as 2% of J_{NO2} (average value of the net effect of both particle and gas-phase photolysis). It should be noted that the implicit assumption in this formulation is that only one carbon atom is lost upon SOA photolysis reaction and not the entire SOA molecule. For more details on the parameterization we refer readers to a previous study by *Hodzic et al.* [2015] that presents a detailed discussion of the comparability of the photolysis rate estimates used in his study with the laboratory-derived estimates of *Henry and Donahue* [2012] and also discussed impact of faster photolysis rates on modeled SOA distributions.

2.3.3 Heterogeneous reaction with ozone

The removal of organic molecules by heterogeneous reactions at the surface of particles was also implemented into the updated GEOS-Chem model. Reported values of the reactive uptake coefficient (γ), which represents the probability that a reaction occurs upon gas-surface collision, span several orders of magnitude. Values of γ for the uptake of OH radicals range 0.1 to 1.0 [*George and Abbatt*, 2010], whereas for NO_3 and O_3 the uptake kinetics vary considerably depending on the phase and chemical composition of the organic surface. Values of γ for heterogeneous reactions of O_3 with unsaturated organics are typically ~10^{-3} for liquid phase organics, and an order of magnitude smaller, 5×10^{-5} to 10^{-4}, for solid organics as the reactants are confined to the surface due to decreased diffusion coefficients into the bulk of the particle [*Moise and Rudich*, 2002; *Hearn and Smith,* 2004]. The O_3 reaction is less efficient with liquid aldehydes and ketones ($\gamma=10^{-4}$, [*De Gouw and Lovejoy,* 1998]), alkanes ($\gamma=2\times10^{-5}$ for hexadecane,

[*Moise and Rudich,* 2000]) or alcohols ($\gamma \leq 10^{-5}$, [*De Gouw and Lovejoy,* 1998]). For NO_3, *Moise et al.* [2002] reported γ values ranging from 1.5×10^{-2} to 3.8×10^{-4} for a variety of organics including alkanes, alkenes, alcohols, and carboxylic acids with saturated and unsaturated bonds.

Given the range of uncertainties, here we estimate the potential effect on SOA removal by OH, NO_3 and O_3 heterogeneous oxidation for typical conditions. Aerosol particles consist of molecules that are reactive with these oxidants. The rate of loss of the gas phase oxidants is equal to

$$\left[\frac{d[oxidant]}{dt}\right]_{het} = 1/4 \times \gamma \times [oxidant] \times < c > \times A \quad (4)$$

where [*oxidant*] is the oxidant concentration, <*c*> is the mean gas-phase speed of the oxidant and *A* is the specific surface area of organic aerosols (per unit volume of air). This formulation does not account for diffusion limitations. We assume that each oxidant lost from the gas phase reacts with one molecule of OA, and that 10% of the OA mass is lost as a result. For $O_3 = 10^{12}$ molecules cm^{-3}, $A = 10^{-5}$ m^2m^{-3}, and $\gamma = 10^{-5}$, the bulk SOA mass loss rate is about 4% per day. For OH, assuming γ values of 0.1-1 and a concentration of 10^6 molecules cm^{-3}, the corresponding SOA loss rate is about 6-60 times slower. For NO_3, assuming $\gamma = 0.01$ and a concentration of 10^7 molecules cm^{-3}, the corresponding SOA loss rate is about 100 times lower than the loss rate due to reaction with O_3.

Given these estimates, we only consider the surface oxidation loss by O_3 with $\gamma = 10^{-5}$ in the GEOS-Chem sensitivity simulations presented in this study. The chosen uptake coefficient is 1-2 orders of magnitude lower than the reported values for unsaturated organics, which accounts for the fact that unsaturated organic compounds are only a

377 minor fraction of the total organic aerosol, and that values for other compounds are
378 $\gamma \leq 2 \times 10^{-5}$. In each grid cell and at each chemical time step, the loss rate of SOA due to
379 heterogeneous oxidation by O_3 is calculated on the basis of the local organic aerosol
380 surface area and O_3 concentration.

381 ### 2.4 Model simulations

382 Five model simulations were performed for the 2005-2008 period. Their characteristics
383 are listed in Table 4. The base-case simulation (REF) corresponds to the model setup as
384 used in the previous simulations by *Jo et al.* [2013] and is typical of other global model
385 studies in which the VBS framework is used. The sensitivity simulations are designed to
386 study the effect of new wall-corrected chamber yields and SOA production from S/IVOCs
387 (NY), updated dry and wet deposition of organic vapors (NY_D), and photolytic (NY_DP)
388 and heterogeneous (NY_DPH) loss of SOA. Each of the sensitivity simulations builds
389 successively on the NY simulation. For example, the NY_DP simulation adds updated
390 Henry's law coefficients and photolytic SOA loss to the new yields simulation, and the
391 NY_DPH adds heterogeneous chemistry SOA loss to the NY_DP simulation (Table 4).
392 The overall effect of new removal pathways on SOA global budgets was estimated by
393 comparing the NY and NY_DPH runs.

394 ### 2.5 Data used for model evaluation

395 #### 2.5.1 Ground measurements

396 Over the continental U.S. model results are evaluated using surface organic carbon
397 (OC) measurements (in $PM_{2.5}$ filter samples collected every 3 days) from the IMPROVE
398 network (Interagency Monitoring of Protected Visual Environments,
399 http://www.epa.gov/ttn/airs/airsaqs). For the comparison, measurements taken from
400 2005 to 2008 are used (more than 76,000 data points), and data were averaged over the
401 entire period for each month. Measurements are mostly representative of rural

402 background OC concentrations since the IMPROVE sites are, for the most part, located
403 in U.S. national parks. Over Europe, the monthly mean observations of OC (in PM_{10}
404 samples) collected at the EMEP (European Monitoring and Evaluation Programme) sites
405 from 2002 to 2003 [*Yttri et al.,* 2007] are used to evaluate GEOS-Chem monthly mean
406 results. We only use data from the rural background sites (see Table S4). Both the
407 IMPROVE and EMEP site measurements determined OC concentrations using thermo-
408 optical methods. During the considered period, the mean OC concentration are 2.5 times
409 larger at the EMEP sites (3.46 μg m^{-3}) than at the IMPROVE sites (1.27 μg m^{-3}), which
410 could be due to a greater proximity of urban and industrial centers. Evaporation of OC
411 from IMPROVE summer samples which are kept in the field for several days and
412 shipped without cooling, could also play a role [*Kim et al.,* 2015].

413 Surface measurements from the Aerosol Mass Spectrometer (AMS) global network for
414 years 2000-2008 (*Zhang et al.* [2007]; https://sites.google.com/site/amsglobaldatabase/)
415 are used to evaluate modeled SOA. The bulk OA observations have been further
416 analyzed through positive matrix factorization to assess contributions from different OA
417 types, or factors, and are divided into two key OA types i.e. oxygenated OOA and
418 hydrocarbon-like HOA. We assume that the observed OOA can be directly compared
419 with model predicted SOA. Multi year (2005-2008) monthly means from the model are
420 compared with the corresponding observations reported at 20 locations including 16
421 rural and 4 background locations (urban site were not considered).

422 ### 2.5.2 Aircraft measurements

423 We use OA measurements from recent aircraft field campaigns [*Heald et al.,* 2011] that
424 took place between 2005 and 2009 to evaluate the vertical distribution of organic
425 aerosols (see Table S5). The comparison is performed for conditions representative of
426 remote (ITOP IMPEX, VOCALS-UK), moderately polluted (SEAC4RS, ADRIEX, TexAQ,

EUCAARI) and biomass burning influenced (ARCTAS) regions. Given the coarse model resolution, data from heavily polluted regions (e.g. Mexico City MILAGRO, Asia ACE-Asia, Borneo OP3) were not considered. In these campaigns, total OA concentrations were measured using the AMS instrument [*Canagaratna et al.,* 2007]. Observations were averaged over each aircraft campaign according to their vertical location and compared to the simulated monthly mean OA vertical profiles in the corresponding month and location in the model. For ARCTAS, the observed OA concentrations above the 99th percentile i.e. larger than 16 μg m^{-3}(STP) (where 'STP' stands for standard conditions of 273 K and 1 atm) were filtered out to limit the influence of biomass burning plumes that the GEOS-Chem model cannot resolve at the considered horizontal resolution. For SEAC4RS, the 80th percentile value of acetonitrile (~140ppt) was used as a cut-off to exclude OA measurements heavily influenced by fire plumes. For three campaigns (ITOP, ADRIEX and SEAC4RS) that occurred outside of the modeled period, we used averaged model values between 2005 and 2008 for the month corresponding to the field project.

3 Results and discussion

3.1 SOA spatial distribution

The spatial distribution of annual mean (2005-2008) concentrations of SOA from various sources (total, biogenic VOC, anthropogenic and biomass burning VOC, and anthropogenic and biomass burning S/IVOCs) in the lower troposphere (ground to 5km agl) as predicted by the GEOS-Chem NY run are shown in Figure 1. The simulated continental background SOA levels in the lower troposphere are typically between 0.2 and 0.5 μg m^{-3}, and the highest concentrations (>2 μg m^{-3}) are predicted over tropical forest regions of Africa and South America. Industrialized and urban areas in China, Europe and the U.S. feature SOA concentrations significantly larger (1-2 μg m^{-3}) than

452 the background. The biggest contribution to SOA worldwide is from biogenic sources.
453 The predicted spatial distribution and amounts of biogenic SOA, with high values over
454 tropical forest regions, are consistent with previous modeling studies [e.g. *Farina et al.,*
455 2010; *Shrivastava et al.,* 2015], and somewhat larger than concentrations estimated by
456 *Spracklen et al.* [2011]. Anthropogenic emissions of traditional hydrocarbons (aromatics
457 and short n-alkanes) contribute up to 0.5 μg m^{-3} over industrialized and urban regions,
458 and about 0.1 μg m^{-3} elsewhere. The contribution of intermediate and semi-volatile
459 anthropogenic compounds, which are not treated in traditional emission inventories, is
460 significant, ranging from 0.1 μg m^{-3} background levels, to 0.5 μg m^{-3} over continental
461 Europe and North America, to 1-2 μg m^{-3} over polluted regions of China and India, and
462 over tropical biomass burning regions in Africa and South America. Spatial patterns and
463 concentrations of SOA predicted from S/IVOCs are within similar to those reported by
464 *Jathar et al.* [2011, Figure 4].

465 ### 3.1.1 Effect of wall-corrected chamber yields

466 Figure 1 also shows the difference between the NY simulation using the vapor wall-loss
467 corrected yields for SOA formation from traditional anthropogenic and biogenic
468 precursors, and the REF simulation using the typical non-corrected yields with artificial
469 aging of intermediate organic vapors produced from anthropogenic precursors as in
470 previous studies [*Farina et al.,* 2010; *Jo et al.,* 2013]. In terms of annual averages, the
471 difference between the two simulations shows an increase in biogenic SOA of ~1 μg m^{-3}
472 over eastern U.S., Australia and southeast Asia, and up to 4-8 μg m^{-3} over SOA hotspots
473 of tropical Africa and South America. This change can be attributed to effectively higher
474 SOA yields and the formation of less volatile SOA as shown in Figure S2. SOA formation
475 from the traditional anthropogenic VOC precursors is decreased in the NY simulation by
476 0.1 to 0.3 μg m^{-3}. The wall-corrected yields for aromatics are lower than the traditional

yields combined with the aging parameter, which were used in the default version of the model (see Figure S2). This difference is primary due to the addition of aging reactions in the REF model, which leads to substantial and likely excessive production of SOA as discussed in *Dzepina et al.* [2011] and *Jathar et al.* [2016]. However, the total anthropogenic fraction is increased in the NY simulation by ~0.5 μg m^{-3} over southeast Asia, and up to ~2 μg m^{-3} over south America and Africa due to the contribution of intermediate and semi-volatile compounds that were only accounted for in the NY simulation. Vertical profiles of SOA concentrations averaged over the entire globe or the continental U.S. (Figure 2) show that SOA production using the vapor wall-loss corrected yields has led to a larger fractional increase of the near surface SOA concentrations (surface to 3km agl), which is the region where the model underprediction is the most severe [*Heald et al.,* 2011].

3.1.2 Effect of removal processes

Figure 3 shows the sensitivity of SOA levels in the boundary layer and in the free troposphere to the three types of removal pathways considered here: dry and wet deposition of organic vapors and aerosols, photolysis, and heterogeneous removal of SOA. Given the relatively short chemical lifetime of SOA compared to typical tropospheric transport time scales, there is a strong correspondence between regions where the surface concentrations are highest and where the free tropospheric concentrations are the highest. Dry and wet removal of gases and particles depends on their water solubility, which is given by the effective Henry's law constant (H^{eff}). For organic gases, H^{eff} has been typically fixed to an arbitrary value in the 10^3-10^5 M atm^{-1} range. The choice of this value can impact SOA predictions [*Bessagnet et al.,* 2010; *Pye and Seinfeld*, 2010; *Ahmadov et al.,* 2012; *Hodzic et al.,* 2014; *Knote et al.,* 2015]. The comparison between the NY simulation, which uses a constant H^{eff} of 10^5 M atm^{-1}

(default value in GEOS-Chem), and the sensitivity NY_D simulation, which uses values determined from the explicit chemical modeling (see Table 2), shows a modest decrease of tropospheric SOA, ranging from of 5 to 10% over water surfaces and from 5 to 20% over continents (Figure 3c,i). This suggests that the overall H^{eff} is somewhat higher than the typical values of 10^5 M atm^{-1} used in global models. Our results are consistent with *Knote et al.* [2015, Figure 9] that showed that over the continental U.S. SOA levels are decreased by ~20% when H^{eff} values based on the explicit chemical modeling were used instead of a constant $H^{eff}=10^5$ M atm^{-1}. The decrease in SOA results from both a more limited formation of SOA from oxidized organic vapors because they are removed, but also from the evaporation of already formed SOA to satisfy thermodynamic equilibrium. The maximum relative reduction is seen over areas where SOA concentrations are the highest. Figure 2 indicates that there are no significant vertical gradients in SOA reduction (comparing NY_D with NY). The relatively modest impact on SOA concentrations with increased H^{eff} beyond 10^5 M atm^{-1} is expected due to saturation effects as already discussed by *Knote et al.,* [2015], and *Hodzic et al.* [2014, Figure S5].

Figures 3d and 3j show the effect of in-particle photolysis reactions on SOA concentrations using the photolytic loss rate of 0.04% J_{NO2} [*Hodzic et al.*, 2015]. Annual mean boundary layer SOA concentrations are typically decreased by 10-30% over continental regions close to sources, and up to 80% over remote regions. Domain averaged SOA vertical profiles shown in Figure 2 illustrate more clearly this vertical gradient. The reduction in SOA concentrations ranges from 20% near surface to 60% above 4km for the NY_DP run compared to the NY_D run. The strong spatial gradient especially between land and water surfaces can be explained by continuous photolytic loss, the effect of which accumulates further away from source regions. Model results

526 show that this loss pathway will play an important role in the regions where wet
527 deposition is not very efficient such as the upper troposphere and lower stratosphere.

528 Figures 3e and 3k show a <5% decrease in SOA boundary layer concentrations over
529 continental areas and a 5-10% decrease over the outflow regions, when the surface
530 oxidation loss by O_3 with $\gamma = 10^{-5}$ is considered. Here we did not consider OH reactions,
531 as our estimates presented in Section 2.3.2 suggest that the reaction rate with OH is one
532 to two orders of magnitude slower than reaction with O_3.

533 The lifetime of SOA with regard to the combined effect of photolytic loss and
534 heterogeneous reactions with ozone is ~6.2 days for biogenic SOA, 6.6 days for SOA
535 from aromatic and short-chain VOCs, and 6.8 days for SOA from S/IVOCs, which is
536 comparable to the lifetime of SOA against wet removal (3.8-7.4 days). We note that the
537 additional effect of heterogeneous loss of SOA in our simulations is small. Our values
538 are also lower than that reported by *Heald et al.* [2011] for SOA heterogeneous removal
539 by OH despite the fact that the inferred global average lifetimes against heterogeneous
540 loss in our simulations (60-70 days) are somewhat lower than the corresponding
541 lifetimes used by *Heald et al.* [2011] (80-90 days). This is due to the relatively rapid loss
542 of SOA by photolysis in our simulations. As a consequence, the inclusion of
543 heterogeneous SOA loss in the NY_DPH simulation reduces SOA lifetimes and burdens
544 by only 4-5% relative the corresponding quantities in the NY_DP simulation.

545 After studying the effect on SOA concentrations of various loss pathways individually, we
546 assess their combined effect by comparing the NY_DPH vs. NY simulations. The results
547 show a ~30-40% reduction in annual mean SOA concentrations within the continental
548 boundary layer, and more than 60% in the outflow remote regions (oceans). A stronger
549 impact on SOA concentrations is found in the free troposphere, with a 40-50% decrease

over continental regions of the Southern Hemisphere, and 60% decrease over continental areas of the Northern Hemisphere. The outflow regions over the Pacific and Atlantic oceans show an 80% decrease in SOA. SOA concentrations in the NY_DPH simulation (with updated treatment of SOA production and removal) range from background concentrations of 0.1 μg m^{-3} over oceans and 0.5-1 μg m^{-3} over continental areas throughout the lower troposphere, to 2-3 μg m^{-3} over urbanized regions of Europe and U.S., and to >4 μg m^{-3} over China, India, and tropical forest regions of Africa and South America (Figure 3b). The relative contribution to SOA concentrations of biogenic, anthropogenic and biomass burning VOC and S/IVOC precursors is shown in Figure S4. We find that biogenic precursors contribute most of the SOA mass in the southern hemisphere, and about ~40% in the northern hemisphere, whereas traditional anthropogenic and biomass burning VOC precursors account for 20-30% over the northern hemisphere, and anthropogenic and biomass burning semi-volatile and intermediate volatility precursors contribute 30-40% over China and its outflow region, and over tropical regions.

3.2 Evaluation of the modeled organic aerosol concentration

The results presented above confirm that the modeled SOA distribution is quite sensitive to the treatment of removal processes. Here, we evaluate the extent to which simulated OA fields using various configurations of the model are consistent with observations. We note that dispersion errors might contribute to discrepancies between observed and modeled OA, but isolating the impact of these errors is difficult [*Arellano et al.* 2006]. We therefore compare model simulations with a broad suite of OA surface and vertical profile measurements to assess the extent to which they provide support for our alternative hypotheses of SOA sources and sinks. We also note that performance with regards to inorganic aerosol components is documented in *Jo et al.* [2013], who find that

575 the simulation results are in general agreement with surface observations of sulfate and
576 ammonium, but that nitrate is overestimated. Model simulations are monthly averaged
577 over the period of 2005-2008, and are compared to the corresponding monthly mean
578 observations taken over multi-year time periods (IMPROVE 2005-2008, EMEP 2002-
579 2003, and AMS 2000-2008). It should be noted that whereas the IMPROVE and EMEP
580 monitoring networks have generally continuous measurements at fixed sites, the AMS
581 measurements are periodic and thus the average in one specific region is likely
582 representative of the particular year. Similar to previous studies, we ignore year-to-year
583 variability [e.g. *Jo et al.,* 2013]. The observed monthly mean concentrations are
584 averaged on the 2 x 2.5 degree model grid. Organic carbon (OC) concentrations have
585 been estimated from the simulated OA concentrations, which are the sum of
586 anthropogenic and biogenic SOA and POA. POA is tracked in the model as primary
587 organic carbon, and SOA mass is converted to organic carbon mass assuming that the
588 OA/OC ratio is 2.1 (similar to previous GEOS-Chem studies [e.g. *Pye and Seinfeld,*
589 2010; *Jo et al.,* 2013].

590 ### 3.2.1 Comparison with surface measurements

591 Figure 4a shows the model evaluation over the continental U.S. with the monthly mean
592 ground OC data from the IMPROVE network. The comparison shows that predicted OC
593 is underestimated by ~10% for the REF run. With the new wall-corrected yields (NY), the
594 predicted OC concentrations are 35% higher than the observed ones, and these
595 overpredictions can reach a factor of 2-3 at some locations. When the photolytic and
596 heterogeneous losses of SOA are included (NY_DPH run), the model is in better
597 agreement with observations for average OC concentrations (bias of ~7%) and slightly
598 better spatiotemporal correlation (R^2=0.49 vs. 0.45). Figure 5a shows that the NY_DPH
599 simulation captures well the magnitude and seasonal variability in OC observations,

600 which are characterized by 2-3 times larger OC concentrations during summer than
601 during winter. The positive bias in NY_DPH seems to occur mainly during summer
602 months (10-20% in August), and could partially be due to evaporation of OC from
603 IMPROVE summer samples during sampling and shipping, which was estimated to be
604 ~25% by *Kim et al.,* [2015]. The other model variants also capture relatively well the
605 seasonal variability, but the absolute values are either severely underpredicted (REF) or
606 overpredicted (NY). The comparison of surface concentrations could also suffer from
607 uncertainties in the boundary layer parameterizations, and it should be noted that the
608 GEOS-5 meteorological analysis were found to reproduce reasonably well (within 25%)
609 the boundary layer height as compared to the CALIPSO data [*Jordan et al.,* 2010].

610 The comparison over Europe with the EMEP data (Figure 4b) shows a more severe
611 model underestimation with a normalized mean bias of -38% for the REF run, and -31%
612 for the NY_DPH run. The correlation coefficient is low (R^2~0.17), possibly due to the
613 comparison of different time periods (measurements 2002-2003). Figure 5b suggests
614 that the observed OC seasonal cycle is very different in Europe than in the U.S., with the
615 highest OC concentrations occurring during winter vs. summer, respectively. Most of the
616 model bias for Europe can be attributed to a severe underprediction of the primary OC
617 during winter months in all model runs. These wintertime OC discrepancies are likely
618 due to underestimated wood-burning contributions as discussed in previous studies [e.g.
619 *Denier van der Gon et al.,* 2015; *Simpson et al.*, 2007].

620 Figure 4c also compares the predicted monthly mean SOA concentrations (averaged
621 over 2005-2008) with the AMS measurements made at 20 locations worldwide [*Zhang et*
622 *al.,* 2007]. Only background and rural sites were considered given the model coarse
623 horizontal resolution. Figure 4c suggest that the REF simulation is underpredicting SOA
624 concentrations by on average ~40% over all sites. Increased production in the NY

simulation leads to a 23% average overprediction of surface SOA. The best agreement is obtained for simulations that accounted for both updated production yields and removal processes (NY_DPH) with a negative model average bias of 14%. Given the coarse model resolution, the most meaningful comparison with the measurements is expected to be with the background sites (blue triangles) at which the NY_DPH simulations is capturing reasonably the observed SOA levels. Again the correlation coefficients for all simulations are low (R^2~0.1) due to differences in time periods.

3.2.2 Comparison with aircraft vertical profiles

Figure 6 compares the mean vertical profiles of OA measured during several aircraft campaigns and predicted by GEOS-Chem. Three of these campaigns are representative of remote conditions (ITOP, IMPEX, VOCALS-UK) whereas the other five were performed to study regional pollution or biomass burning plumes (EUCAARI, ARCTAS, TexAQS, ADRIEX, SEAC4RS). It should be kept in mind that the model resolution is too coarse to correctly represent typical biomass burning plume structures and spatial gradients. The base case model (REF) typically underestimates observed OA concentrations in the lower troposphere and overestimates in the upper troposphere in most regions. This difficulty in capturing the vertical distribution of OA is particularly noticeable for the IMPEX and EUCAARI data. Increasing the SOA production (NY) leads to much larger concentrations at all altitudes, resulting sometimes in a better agreement with observations near the surface (SEAC4RS, TexAQS, EUCAARI), but also often in a model overprediction of surface concentrations (ARCTAS, ADRIEX, VOCALS-UK). The overprediction of the upper troposphere OA concentrations is systematic in all environments for the NY run, suggesting that additional removal processes may be occurring. This overestimation in the free troposphere was seen in previous studies as well when the SOA production was artificially increased [e.g. *Hodzic et al.,* 2010; *Heald*

650 *et al.,* 2011; *Shrivastava et al.,* 2011; *Shrivastava et al.,* 2015]. The model better
651 captures the shape of the OA vertical profile when photolytic and heterogeneous
652 removals are included. This improvement is seen for most campaigns. With the
653 NY_DPH run, higher concentrations are simulated in the boundary layer than with the
654 REF simulations reducing the gap with observations, while the model overprediction in
655 the upper troposphere is reduced compared to the NY run. The globally averaged ratio
656 between the predicted SOA by the updated NY_DPH, and the default REF model
657 simulations is also shown in Figure 2, and indicates that the updated SOA scheme leads
658 up to a 50% increase in near surface SOA concentrations, and up to a 60% decrease in
659 the upper troposphere.

660 ### 3.2.3 Comparison with satellite AOD measurements

661 Figure 7 compares aerosol optical depth (AOD) at 550nm simulated by the GEOS-Chem
662 base case (REF) and modified (NY_DPH) runs with the corresponding retrievals from
663 the MODIS (MODerate resolution Imaging Spectrometers) Terra and Aqua satellites
664 between 2005 and 2008. The largest mean AOD levels (>0.5) are observed over
665 Northern Africa due to dust emissions, and over China and India in relation to
666 anthropogenic activities. As the AOD variable accounts for all aerosols including the
667 aerosol water, its sensitivity to SOA parameterizations is only going to be significant over
668 regions where SOA is the major contributor to the total aerosol load. Figure 7d shows
669 the contribution of OA to the simulated total AOD by the NY_DPH run. The predicted
670 AOD is particularly sensitive to organic aerosols with contribution of >60% over the
671 Amazon, South Africa and Southeast Asia. These regions are also strongly influenced
672 by biomass burning and a large fraction of OA is likely from POA emissions. Over the
673 continental U.S. and Europe the sensitivity is somewhat lower with OA contribution of
674 10-30% to the calculated AOD. The relative OA contribution to AOD is increased by 5-

675 10% in the NY_DPH simulation relative to the base case run (not shown here). This
676 increased OA contribution to the total aerosol load (predicted by NY_DPH) is consistent
677 with the global AMS surface observations reported by *Zhang et al.* [2007] in which OA
678 accounts for more than 35% of the submicron aerosol at the surface. Our results are
679 also consistent with the modeling study by *Kim et al.* [2015] who found that OA
680 contributed about ~40% of the total AOD over the southeast U.S. during the SEAC4RS
681 field project. It should be noted that regions that are dominated by OA (contribution to
682 AOD >50%) are not the ones displaying the largest biases in AOD, although the
683 contribution of OA could be underpredicted.

684 The comparison of seasonal AOD cycles over the U.S. (Figure 7f) shows a relatively
685 small model bias during winter months, and a large model underestimation in summer
686 (up to 50%). Even though the relative contribution of OA to the total AOD is higher
687 during summer 25-35% (consistent with *Zhang et al.* [2007]) the OA fraction is likely
688 underestimated. The seasonal variability and aerosol load predicted by the NY_DPH run
689 are particularly well captured over South America, and are within a factor of two of
690 observed AODs over central Africa.

691 **3.3 Global annual budgets**

692 Global 2005-2008 annual-average budgets showing the mass burden and source/sink
693 terms for the combined gas- and particle-phase SOA system are presented in Table 5
694 and Figure 8 for the REF, NY, and NY_DPH simulations. We assess individual and
695 combined effects of the various sink processes considered on global SOA burdens by
696 examining diagnosed process lifetimes (see Table 6).

697 As expected, the SOA particle burden is largest in the NY simulation (2.31 Tg), which is
698 a factor of 2.6 higher than the corresponding burden in the REF simulation. This large

699 increase is caused by two factors: (i) the increased production (228 Tg yr^{-1} vs. 155 Tg yr^{-1})
700 and lower volatility (43% vs. 14% net conversion of oxygenated gas-phase VOCs to
701 particle-phase) of biogenic SOA constituents in the NY simulation relative to the REF
702 simulation, and (ii) the additional source in the NY simulation of 27.7 Tg yr^{-1} oxygenated
703 VOC gases from IVOC oxidation, which largely partition to the particle-phase (net
704 conversion of >90% to particle-phase) owing to their low volatility (see Table 1). These
705 two factors more than offset the decrease in SOA from traditional anthropogenic
706 precursors (discussed in section 3.2.1; see panel showing decrease in anthropogenic
707 SOA in the NY simulation relative to the REF simulation in Figure 1) and the lower
708 biogenic SOA particle lifetimes in the NY simulation relative to the REF simulation.

709 For the REF and NY simulations (which have identical loss parameterizations), SOA
710 removal is dominated by wet deposition (70-80% of total sink), with dry deposition
711 playing a minor role in determining the overall SOA removal lifetime. This is generally
712 consistent with previous global model studies, which do not consider photochemical
713 losses of organics or use H^{eff} in the 10^3-10^5 M atm^{-1} range (see for example, the multi-
714 model intercomparison by *Tsigaridis et al.* [2013]). Comparing the NY_DPH simulation
715 with the NY simulation shows that using the updated Henry's coefficients results in more
716 efficient dry deposition of biogenic oxygenated VOC gases thereby shifting the balance
717 between dry and wet deposition as the primary sink of these gases, and lowering the
718 overall lifetime of both gas- and particle-phase constituents.

719 While the particle-phase production rate in the NY_DPH simulation is comparable to the
720 production rate in the NY simulation, the overall particle phase lifetime is significantly
721 lower in the NY_DPH simulation due to the photolytic loss of particle-phase SOA at rates
722 comparable to wet deposition rates. As a consequence, the particle-phase burden in the
723 NY_DPH simulation (0.88 Tg) is significantly lower than in the NY simulation (2.31 Tg).

724 It is also worth noting that global-average particle-phase burdens in the REF and
725 NY_DPH simulations are comparable. However, the NY_DPH simulation presents a far
726 more dynamic picture, with stronger production rates and more efficient removal leading
727 to very different, and likely more realistic, horizontal and vertical spatial patterns in the
728 SOA distribution relative to the REF simulation as discussed in the previous sections.

729 Our best estimate of the global SOA particle-phase production rate is 132.2 Tg yr^{-1},
730 which is remarkably similar to the central estimate of 140 Tg yr^{-1} derived by *Spracklen et*
731 *al.* [2011] using a top-down approach constrained by a global dataset of surface AMS
732 measurements (Figure 9). *Spracklen et al.* [2011] further estimate that a large fraction
733 (100 Tg yr^{-1}) is anthropogenically-controlled, but from non-fossil sources of carbon.
734 While we cannot estimate an equivalent anthrogenically-controlled source fraction in our
735 study, our estimate of the biogenic source (97.5 Tg yr^{-1}) is also consistent with the
736 *Spracklen et al.* [2011] estimate of the non-fossil source magnitude. It is worth noting
737 however that our simulated global burden of 0.88 Tg in the NY_DPH simulation is about
738 a factor of 2 lower than in the *Spracklen et al.* [2011] study because of the shorter
739 aerosol lifetimes due to the inclusion of particle-phase photolysis in our simulations.

740 Our best estimate of the particle-phase SOA source is also a factor of 3-4 higher than
741 the central estimate from the AeroCom Phase II multi-model intercomparison exercise
742 [*Tsigaridis et al.,* 2014] though our calculated global burden is comparable owing to the
743 corresponding shorter aerosol lifetimes in our NY_DPH simulation. By contrast, our best
744 source estimate is about a factor of 2 lower than the upper limit estimate of 300 Tg yr^{-1}
745 (assuming a 2:1 OA/OC mass ratio) derived by *Heald et al.* [2010] using continental
746 AOD retrievals from MISR. This is despite the fact that the aerosol lifetimes in the *Heald*
747 *et al.* [2010] study are about a factor of 2 lower than in the NY_DPH simulation. While
748 we cannot compare directly to their study, we speculate that a portion of this apparent

749 discrepancy is due to the simplifying assumption by *Heald et al*. [2010] that the scale
750 height of the atmosphere (~7.5km) can be used to characterize the exponentially
751 decreasing vertical profile of OA. This differs significantly from the much steeper vertical
752 gradient, corresponding to a scale height of about 2.5km, in the NY_DPH simulation
753 (see Figure 2), which provides the best match to aircraft vertical profiles as discussed in
754 Section 3.2.2. As noted by *Heald et al.* [2010], for a given column loading of dry aerosol
755 mass, AOD is higher when a greater fraction of the aerosol mass is near the surface due
756 to increased water uptake. As a consequence, a lower source strength can be consistent
757 with measured AOD if a greater fraction of aerosol mass is near the surface.

758 We also note that the upper limit contribution of the biomass burning source to SOA
759 formation in the updated NY_DPH model is ~15.5 Tg yr^{-1} (14 Tg yr^{-1} produced from
760 I/SVOC precursors, and ~1.5 Tg yr^{-1} from aromatics). Compared to estimates from the
761 earlier field campaign analysis (Figure 9), our results are within the range of values
762 reported by *Cubison et al.* [2011] who suggested the biomass burning contribution to
763 SOA of ~8 (±7) Tg yr^{-1}, and are consistent with *Jolleys et al.* [2012] who found a small
764 production of organic aerosols in biomass burning plumes. Compared to recent global
765 modeling studies (Figure 9), our estimates are much lower than those reported by
766 *Shrivastava et al.* [2015] (~64 Tg yr^{-1} from biomass burning), and are comparable to
767 those of *Spracklen et al.* [2011] who estimated the biomass burning SOA source of 3 Tg
768 yr^{-1} from direct emissions of its precursors and an additional 23 Tg yr^{-1} from conversion
769 of POA (mostly from biomass burning). The anthropogenic SOA source from traditional
770 aromatic precursors present in the emission inventories is ~7 Tg yr^{-1} in the updated
771 NY_DPH model, and is comparable to estimates provided by previous studies i.e. 10 Tg
772 yr^{-1} [*Spracklen et al.* 2011], and 13.5 Tg yr^{-1} [*de Gouw and Jimenez*, 2009].

3.4 Atmospheric and societal implications

3.4.1 Effect on health exposure

Changes in SOA spatial distribution resulting from the updated representation of production and removals rates were discussed in Section 3.1. On a global-average basis, Figure 2 shows that surface SOA concentrations increase from ~0.25 μg m^{-3} in the REF simulation to ~0.5 μg m^{-3} in the NY_DPH simulation. From a human health exposure perspective, it is important to assess the extent to which spatial changes in simulated SOA concentrations overlap with the spatial distribution of population and how these changes translate into changes in estimated health impacts. A detailed analysis of health impacts is beyond the scope of this paper, and would require higher resolution model predictions. Here, we focus on a simple metric to characterize human-health relevant changes in surface SOA concentrations, and identify broad regions where these changes could have an impact. For each simulation, we calculate the global-average population-weighted surface SOA concentration $[PWSOA]_{surf}$ by combining 2005-2008 annual average modeled surface SOA fields with gridded population data for 2005 (http://sedac.ciesin.columbia.edu). We find that $[PWSOA]_{surf}$ for the NY_DPH simulation is 2.6 μg m^{-3} which is a factor of 2 higher than the corresponding metric for the REF simulation. Figure 10 shows the contribution of individual model grid cells to $[PWSOA]_{surf}$ for the NY_DPH simulation, as well as the contribution to changes in $[PWSOA]_{surf}$ between the NY_DPH and REF simulations. Comparing the top panel of Figure 10 with Figure 3b shows that while highest-boundary layer SOA concentrations are found in tropical Africa and South America, high population regions in east and southeast Asia contribute the most to $[PWSOA]_{surf}$. These are also the regions that contribute the most to changes in $[PWSOA]_{surf}$ between the NY_DPH and REF simulations.

797 Recent analysis by *Lim et al.* [2012] and future projections by *Lelieveld et al.* [2015]
798 suggest that current and future impacts of particulate pollution on human health are and
799 will be significant. The simple analysis presented here suggests the need for a more in-
800 depth study to evaluate the contribution of SOA to PM-related human health effects in
801 order to better understand how SOA precursor controls can serve to mitigate these
802 negative effects.

803 ### 3.4.2 Direct radiative effect

804 The clear-sky direct radiative effect (DRE) of SOA at the top of the atmosphere is
805 estimated for the GEOS-Chem NY_DPH simulation to assess the potential radiative
806 effects of the modeled updates in production and removal of organic aerosols (Figure
807 11). DRE is calculated offline from the GEOS-Chem model outputs using the rapid
808 radiative transfer model for GCMs (RRTMG, [*Iacono et al.,* 2008]). We use 14
809 wavelength bands ranging from 300 to 8021 nm. RRTMG uses the AOD, single
810 scattering albedo and asymmetry parameter for each aerosol type to determine aerosol
811 impacts on radiation. Furthermore, RRTMG requires surface albedo inputs, and these
812 inputs are from MERRA reanalysis [*Rienecker et al.,* 2011]. Aerosol optical properties at
813 a specific wavelength are calculated from the GEOS-Chem output using FlexAOD [*Curci*
814 *et al.,* 2015], which is based on the Mie theory [Wiscombe, 1980]. SOA is assumed to
815 follow log-normal distributions with microphysical properties from OPAC dataset [*Hess et*
816 *al.,* 1998]. The meteorological input data needed for FlexAOD are from GEOS-5
817 assimilated meteorological data.

818 The area-weighted global mean clear-sky DRE value is -0.33 W m^{-2} in the updated
819 NY_DPH simulation, which has a fairly comparable cooling effect at the top of the
820 Earth's atmosphere to the one found for the REF simulation of -0.37 W m^{-2}. Although the
821 global value is similar between the two runs, the spatial distribution is very different. In

822 the NY_DPH simulation, DRE ranges from -0.01 to -0.1 W m^{-2} over the background and
823 to -0.2 W m^{-2} over the outflow oceanic regions, -0.5 to -1 W m^{-2} over the Continental U.S.
824 and Europe, to -2 to -5 W m^{-2} over the SOA source regions including South America,
825 Central and South Africa, Southeast Asia and Southeast U.S. Compared to the REF
826 simulation, DRE is significantly increased over the source regions, and decreased over
827 the remote regions, which is consistent with a stronger SOA production and a shorter
828 SOA lifetime in the NY_DPH simulation as previously discussed. These differences are
829 expected to modify atmospheric stability and affect the cloud formation [*IPCC, Forster et*
830 *al.,* 2007]. The estimated DRE associated with SOA (-0.33 W m^{-2} in NY_DPH) is within
831 the range of recently reported values of -0.26 W m^{-2} [*Spracklen et al.,* 2011], -0.28 W m^{-2}
832 [*Jo et al.,* 2013], -0.5 W m^{-2} and -0.26 W m^{-2} [*Shrivastava et al.,* 2015]. The estimated
833 DRE is larger than in other studies i.e. -0.94 W m^{-2} (NY simulation) when only the
834 updates to the production rates are considered, These values also suggest that
835 additional removals are likely occurring within the entire tropospheric column.

836 **4 Conclusions**

837 Current global models do not reproduce important features of the observed OA
838 distribution, particularly with regards to the relative gradient in SOA concentrations
839 between the boundary layer and the free troposphere. Here, we have presented a
840 revised picture of atmospheric SOA that involves stronger production rates and more
841 efficient sinks that were implemented within the GEOS-Chem model. Together, these
842 updates help overcome some of the limitations that current models have in simulating
843 tropospheric SOA.

844 SOA production with new wall-corrected yields and emissions of semi-volatile and
845 intermediate volatility organic species is substantially increased relative to the default

GEOS-Chem simulation. Our best estimate of the global SOA particle-phase production rate is 132.2 Tg yr^{-1} which is remarkably similar to the central estimate of 140 Tg yr^{-1} derived by *Spracklen et al.* [2011] using a top-down approach constrained by a global dataset of surface AMS measurements. The largest contribution to SOA production is from biogenic sources (~74%, 97.5 Tg yr^{-1}) with the remainder from anthropogenic and biofuel sources (~15%, ~13 Tg yr^{-1} from I/SVOC precursors and ~7 Tg yr^{-1} from aromatics), and biomass burning sources (~11%, 13 Tg yr^{-1} from I/SVOC precursors and ~1.5 Tg yr^{-1} from aromatics). However, stronger production rates alone lead to an overprediction of the surface SOA concentrations relative to measurements from the AMS global network data, and to an accumulation of SOA in the upper troposphere, which is not supported by vertical OA profiles measured by recent aircraft studies. The corresponding global SOA burden is 2.31 Tg and the corresponding direct radiative effect at top of the atmosphere is -0.94 W m^{-2}, which is larger than in previous studies.

The inclusion of new and updated removal processes substantially reduces OA concentrations near the surface and in the free troposphere, and generally leads to an improved agreement with measured vertical profiles from aircraft campaigns (although data are still sparse to allow for a definitive conclusion at this point). We find that photolytic removal could account for ~38% of the direct removal of the particle-phase SOA, and serve as an important loss mechanism in the free troposphere where wet and dry deposition of OA is less efficient. The simulated global OA burden is similar between the updated (0.88 Tg) and the base case (0.88 Tg) GEOS-Chem model configurations, and also similar to the central estimate simulated by the AeroCom Phase II models [*Tsigaridis et al.,* 2014]. Thus, our analysis suggests that the suite of AeroCom models underestimate SOA production rates, and overestimate SOA lifetimes.

In the revised model with both updated sinks and sources, near surface SOA concentrations (global averaged) are increased by up to 50% (within the 1st kilometer), whereas the upper troposphere concentrations are decreased by up to 60%. One implication of this change is that the new model yields a population-weighted global mean SOA concentration that is twice as large as the base model, suggesting the need for a revaluation of human health impacts from ambient OA pollution. Changes in the clear-sky direct radiative effects at the top of the atmosphere are not substantial in terms of global averaged values with -0.33 W m^{-2} for the updated simulation, however the spatial distribution is very different, which could lead to changes in local climate impacts.

We have shown that the combination of missing precursor emissions, new production rates and removal processes leads to qualitative (and sometimes quantitative) improvements in simulating SOA, especially in terms of the vertical OA distribution. While initial comparisons with the limited available measurements are encouraging, uncertainties remain in the proposed source and sink parameterizations. One should keep in mind that the proposed VBS parameterization for the VOCs are derived from empirical fitting of laboratory experiments, which are performed on individual precursors and are highly dependent on experimental conditions. Further work is thus needed to fully understand the limitations associated with the use of the chamber-based SOA yields available for a small subset of surrogate precursors in 3D models to represent complex atmospheric mixtures and ambient conditions. Although we have considerably improved the emissions of SOA precursors for the purpose of this study by adding S/IVOC emissions, we note that large uncertainties remain in emission inventories of biogenic and anthropogenic precursors [*Goldstein and Galbally*, 2007]. We also recognize that our study has accounted for a subset of known SOA formation pathways, leaving out in particular the potentially important aqueous-phase formation of SOA in

clouds droplets and wet particles [e.g. *Ervens et al.,* 2011; *Knote et al.,* 2014], or the condensed-phase processes that lead to the formation of low-volatility compounds [e.g. *Shiraiwa et al.,* 2013]. Another important uncertainty pertains to SOA photolysis rates. To the extent that atmospheric SOA photolysis rates seem to be in the lower range of estimates reported from limited laboratory studies, SOA production rates may need to be higher to explain the observed SOA distribution. An important next step therefore is to reconcile laboratory and theoretical estimates of SOA photolysis rates. More field measurements are also needed to better characterize and evaluate boundary layer vs. free troposphere gradients in various source regions and in the remote atmosphere to further test our hypothesis.

Acknowledgements

The authors thank Shantanu Jathar (Colorado State University) for helpful discussions on the emissions, Eric Apel (NCAR) for discussion on acetonitrile data, Pengfei Yu (University of Colorado) for assistance with the AMS data extraction, Christoph Knote (LMU) for providing the analysis tools used SI Annex-2, and Louisa Emmons and Pablo Saide (NCAR) for the NCAR internal review of our manuscript. The AMS global database is located at https://sites.google.com/site/amsglobaldatabase/. This research was supported by the National Center for Atmospheric Research, which is operated by the University Corporation for Atmospheric Research on behalf of the National Science Foundation. We would like to acknowledge high-performance computing support from Yellowstone provided by NCAR's Computational and Information Systems Laboratory. AH was supported by EPA STAR 83587701-0 and NASA NNX15AE38G, and JLJ was supported by EPA STAR 83587701-0 and NASA NNX15AH33A. This paper has not been formally reviewed by EPA. The views expressed in this document are solely those of the authors and do not necessarily reflect those of the Agency.

References

Ahmadov, R., McKeen, S. A., Robinson, A. L., Bahreini, R., Middlebrook, A. M., Gouw, J. A. de, Meagher, J., Hsie, E.Y., Edgerton, E., Shaw, S., and Trainer, M.: A volatility basis set model for summertime secondary organic aerosols over the eastern United States in 2006, J. Geophys. Res., 117, D06301, doi:10.1029/2011JD016831, 2012.

Arellano, A. F., Jr., P. S. Kasibhatla, L. Giglio, G. R. van der Werf, J. T. Randerson, and G. J. Collatz: Time-dependent inversion estimates of global biomass-burning CO emissions using Measurement of Pollution in the Troposphere (MOPITT) measurements, J. Geophys. Res., 111, D09303, doi:10.1029/2005JD006613, 2006.

931 Aumont, B., Szopa, S., and Madronich S.: Modeling the evolution of organic carbon
932 during its gas-phase tropospheric oxidation: development of an explicit model based on
933 a self generating approach, Atmos. Chem. Phys., 5, 2497-2517, 2005.

934 Bessagnet, B., Seigneur, C., Menut, L. Impact of dry deposition of semi-volatile organic
935 compounds on secondary organic aerosols. Atmos. Environ. 44, (14), 1781–1787, 2010.

936 Bey, I., Jacob, D.J., Yantosca, R.M., Logan, J.A., Global modeling of tropospheric
937 chemistry with assimilated meteorology e model description and evaluation. J Geophys.
938 Res. 106, 073-023,095, 2001.

939 Bond, T.C., Bhardwaj, E., Dong, R., Jogani, R., Jung, S., Roden, C., Streets, D.G.,
940 Trautmann, N.M., Historical emissions of black and organic carbon aerosol from energy-
941 related combustion, 1850-2000. Glob. Biogeochem. Cycles 21, 2007.

942 Cappa, C.D., and Wilson K.R., Multi-generation gas-phase oxidation, equilibrium
943 partitioning, and the formation and evolution of secondary organic aerosol. Atmos Chem
944 Phys 12:9505–9528, 2012.

945 Cappa, C.D., Jathar, S.H., Kleeman, M.J., Jimenez, J.L., Docherty, K., Seinfeld, J.H.,
946 Wexler, A.S., Simulating Secondary Organic Aerosol in a Regional Air Quality Model
947 Using the Statistical Oxidation Model: 2. Assessing the Influence of Vapor Wall Losses.
948 Atmos. Chem. Phys. Discuss. In press., 2016.

949 Canagaratna, M.R., Jayne, J.T., Jimenez, J.L., Allan, J.D., Alfarra, M.R., Zhang, Q.,
950 Onasch, T.B., Drewnick, F., Coe, H., Middlebrook, A., Delia, A., Williams, L.R., Trimborn,
951 A.M., Northway, M.J., DeCarlo, P.F., Kolb, C.E., Davidovits, P. and Worsnop, D.R.,
952 Chemical and microphysical characterization of ambient aerosols with the aerodyne
953 aerosol mass spectrometer. Mass Spectrom. Rev., 26: 185–222. doi:
954 10.1002/mas.20115, 2007.

955 Chung, S., and Seinfeld, J., Global distribution and climate forcing of carbonaceous
956 aerosols. J. Geophys. Res. 107, 4407, 2002.

957 Cubison, M. J., Ortega, A. M., Hayes, P. L., Farmer, D. K., Day, D., Lechner, M. J.,
958 Brune, W. H., Apel, E., Diskin, G. S., Fisher, J. A., Fuelberg, H. E., Hecobian, A., Knapp,
959 D. J., Mikoviny, T., Riemer, D., Sachse, G. W., Sessions, W., Weber, R. J., Weinheimer,
960 A. J., Wisthaler, A., and Jimenez, J. L.: Effects of aging on organic aerosol from open
961 biomass burning smoke in aircraft and lab studies, Atmos. Chem. Phys., 11, 12049-
962 12064, doi:10.5194/acp-11-12049-2011, 2011.

963 Curci, G., Hogrefe, C., Bianconi, R., Im, U., Balzarini, A., Baró, R., Brunner, D., Forkel,
964 R., Giordano, L., Hirtl, M., Honzak, L., Jiménez-Guerrero, P., Knote, C., Langer, M.,
965 Makar, P. A., Pirovano, G., Pérez, J. L., San José, R., Syrakov, D., Tuccella, P.,
966 Werhahn, J., Wolke, R., Žabkar, R., Zhang, J., and Galmarini, S.: Uncertainties of
967 simulated aerosol optical properties induced by assumptions on aerosol physical and
968 chemical properties: An AQMEII-2 perspective, Atmospheric Environment, 115, 541-552,
969 2015.

970 de Gouw, J.A., and E.R. Lovejoy, Reactive uptake of ozone by liquid organic
971 compounds, Geophys. Res. Lett., 25, 931-934, 1998.

972 de Gouw, J. A., and J. L. Jimenez, Organic aerosols in the Earth's atmosphere, Environ.
973 Sci. Technol., 43, 7614-7618, doi:10.1021/es9006004, 2009.

974 Denier van der Gon, H. A. C., Bergström, R., Fountoukis, C., Johansson, C., Pandis, S.
975 N., Simpson, D., and Visschedijk, A. J. H.: Particulate emissions from residential wood
976 combustion in Europe – revised estimates and an evaluation, Atmos. Chem. Phys., 15,
977 6503-6519, doi:10.5194/acp-15-6503-2015, 2015.

978 Dzepina, K., C.D. Cappa, R.M. Volkamer, S. Madronich, P.F. DeCarlo, R.A. Zaveri, and
979 J.L. Jimenez. Modeling the Multiday Evolution and Aging of Secondary Organic Aerosol

During MILAGRO 2006. Environmental Science & Technology, 45, 3496-3503, doi:10.1021/es103186, 2011.

Ehn, M., Thornton, J. A., Kleist, E., Sipila, M., Junninen, H., Pullinen, I., Springer, M., Rubach, F., Tillmann, R., Lee, B., Lopez- Hilfiker, F., Andres, S., Acir, I.-H., Rissanen, M., Jokinen, T., Schobesberger, S., Kangasluoma, J., Kontkanen, J., Nieminen, T., Kurten, T., Nielsen, L. B., Jorgensen, S., Kjaergaard, H. G., Canagaratna, M., Maso, M. D., Berndt, T., Petaja, T., Wahner, A., Kerminen, V.-M., Kulmala, M., Worsnop, D. R., Wildt, J., Mentel, T. F. A large source of low-volatility secondary organic aerosol. Nature, 506 (7489), 476−479, doi:10.1038/nature13032, 2014.

Epstein, S.A., Blair, S.L., and Nizkorodov, S.A., Direct Photolysis of α-Pinene Ozonolysis Secondary Organic Aerosol: Effect on Particle Mass and Peroxide Content, Environ. Sci. Technol., Article Environ. Sci. Technol., 2014, 48 (19), pp 11251–11258, DOI: 10.1021/es502350u, 2014.

Epstein, S.A., Riipinen, I., Donahue, N.M., A Semiempirical Correlation between Enthalpy of Vaporization and Saturation Concentration for Organic Aerosol, Environ. Sci. Technol., 44 (2), 743-748 DOI: 10.1021/es902497z, 2010.

Ervens, B. et al.: Secondary organic aerosol formation in cloud droplets and aqueous particles (aqSOA): a review of laboratory, field and model studies. Atmos. Chem. Phys, 11(21), 11069-11102, 2011.

Farina, S.C., Adams, P.J., Pandis, S.N., Modeling global secondary organic aerosol formation and processing with the volatility basis set: implications for anthropogenic secondary organic aerosol. J. Geophys. Res. 115, D09202, 2010.

Farmer, Q. Chen, J.R. Kimmel, K.S. Docherty, E. Nemitz, P.A. Artaxo, C.D. Cappa, S.T. Martin, and J.L. Jimenez. Chemically-resolved particle fluxes over tropical and

1004 temperate forests. Aerosol Science and Technology, 47, 818-830,
1005 DOI:10.1080/02786826.2013.791022, 2013.

1006 Forster, P.V., Ramaswamy, P., Artaxo, T., Berntsen, R., Betts, D.W., Fahey, J.,
1007 Haywood, J., Lean, D.C., Lowe, G., Myhre, J., Nganga, R., Prinn, G., Raga, M.S.,
1008 Dorland, R.V., Changes in Atmospheric Constituents and in Radiative Forcing.
1009 Cambridge University Press, United Kingdom and New York, NY, USA, 2007.

1010 George, I.J. and Abbatt, J.P.D. Chemical evolution of secondary organic aerosol from
1011 OH-initiated heterogeneous oxidation. Atmos. Chem. Phys. 10, 5551–5563, 2010.

1012 Gentner DR, et al., Elucidating secondary organic aerosol from diesel and gasoline
1013 vehicles through detailed characterization of organic carbon emissions. Proc Natl Acad
1014 Sci USA 109(45):18318–18323, 2012.

1015 Goldstein, A. H. and Galbally, I. E.: Known and unexplored organic constituents in the
1016 earth's atmosphere, Environ. Sci. Technol., 41, 1514–1521, 2007.

1017 Guenther, A., Jiang, X., Heald, C., Sakulyanontvittaya, T., Duhl, T., Emmons, L., Wang,
1018 X., The model of emissions of gases and aerosols from nature version 2.1 (MEGAN2. 1):
1019 an extended and updated framework for modeling biogenic emissions. Geosci. Model
1020 Dev. 5, 1471e1492, 2012.

1021 Heald, C.L., Coe, H., et al. Exploring the vertical profile of atmospheric organic aerosol:
1022 comparing 17 aircraft field campaigns with a global model. Atmos. Chem. Phys. 11,
1023 12673–12696, 2011.

1024 Heald, C. L., D. A. Ridley, S. M. Kreidenweis, and E. E. Drury, Satellite observations cap
1025 the atmospheric organic aerosol budget, Geophys. Res. Lett., 37, L24808,
1026 doi:10.1029/2010GL045095, 2010.

1027 Hearn J.D., and Smith G.D., Kinetics and Product Studies for Ozonolysis Reactions of
1028 Organic Particles Using Aerosol CIMS, J. Phys. Chem. A, 2004, 108 (45), pp. 10019–
1029 10029, DOI: 10.1021/jp0404145, 2004.

1030 Henry K.M. and Donahue, N.M. Photochemical Aging of α-Pinene Secondary Organic
1031 Aerosol: Effects of OH Radical Sources and Photolysis. J. Phys. Chem. A 116 (24),
1032 5932–5940, 2012.

1033 Hess, M., Koepke, P., and Schult, I.: Optical properties of aerosols and clouds: The
1034 software package OPAC, Bulletin of the American meteorological society, 79, 831-844,
1035 1998.

1036 Hodzic, A., Madronich, S., Kasibhatla, P.S., Tyndall, G., Aumont, B., Jimenez, J.L., Lee-
1037 Taylor, J., and J. Orlando, Organic photolysis reactions in tropospheric aerosols: Effect
1038 on secondary organic aerosol formation and lifetime, Atmos. Chem. Phys., 15, 9253-
1039 9269, 2015.

1040 Hodzic, A., Aumont, B., Knote, C., Lee-Taylor, J., Madronich, S., and Tyndall, G.,
1041 Volatility dependence of Henry's law constants of condensable organics: Application to
1042 estimate depositional loss of secondary organic aerosols. Geophysical Research
1043 Letters, 41, doi: 10.1002/2014GL060649, 2014.

1044 Hodzic, A., Jimenez, J. L., Madronich, S., Canagaratna, M. R., DeCarlo, P. F., Kleinman,
1045 L., and Fast, J.: Modeling organic aerosols in a megacity: potential contribution of semi-
1046 volatile and intermediate volatility primary organic compounds to secondary organic
1047 aerosol formation, Atmos. Chem. Phys., 10, 5491–5514, doi:10.5194/acp-10-5491-2010,
1048 2010.

1049 Jathar, S. H., Farina, S. C., Robinson, A. L., and Adams, P. J.: The influence of semi-
1050 volatile and reactive primary emissions on the abundance and properties of global

1051 organic aerosol, Atmos. Chem. Phys., 11, 7727-7746, doi:10.5194/acp-11-7727-2011,
1052 2011.

1053 Jathar, S.H., Gordon, T.D., Hennigan, C.J., et al., Unspeciated organic emissions from
1054 combustion sources and their influence on the secondary organic aerosol budget in the
1055 United States, Proceedings of the National Academy of Sciences 111 (29), 10473-
1056 10478, 2014.

1057 Jathar, S.H., Cappa, C.D., Wexler, A.S., Seinfeld, J.H., and M.J. Kleeman, Simulating
1058 Secondary Organic Aerosol in a Regional Air Quality Model Using the Statistical
1059 Oxidation Model: 1. Assessing the Influence of Constrained Multi-generational Ageing,,
1060 Atmos. Chem. Phys., 16, 2309-2322, doi:10.5194/acp-16-2309-2016, 2016.

1061 Jo, D.S., Park, R.J., Kim, M.J., Spracklen, D.V., Effects of chemical aging on global
1062 secondary organic aerosol using the volatility basis set approach, Atmos. Environ., 81,
1063 230-244, 2013.

1064 Jolleys, M. D., et al., Characterizing the aging of biomass burning organic aerosol by use
1065 of mixing ratios: A meta-analysis of four regions, Environ. Sci. Technol., 46(24), 13,093–
1066 13,102, doi:10.1021/es302386v, 2012.

1067 Jordan, N. S., R. M. Hoff, and J. T. Bacmeister: Validation of Goddard Earth Observing
1068 System–version 5 MERRA planetary boundary layer heights using CALIPSO, J.
1069 Geophys. Res., 115, D24218, doi:10.1029/2009JD013777, 2010.

1070 Kim, P. S., Jacob, D. J., Fisher, J. A., Travis, K., Yu, K., Zhu, L., Yantosca, R. M.,
1071 Sulprizio, M. P., Jimenez, J. L., Campuzano-Jost, P., Froyd, K. D., Liao, J., Hair, J. W.,
1072 Fenn, M. A., Butler, C. F., Wagner, N. L., Gordon, T. D., Welti, A., Wennberg, P. O.,
1073 Crounse, J. D., St. Clair, J. M., Teng, A. P., Millet, D. B., Schwarz, J. P., Markovic, M. Z.,
1074 and Perring, A. E.: Sources, seasonality, and trends of Southeast US aerosol: an
1075 integrated analysis of surface, aircraft, and satellite observations with the GEOS-Chem

1076 chemical transport model, Atmos. Chem. Phys., 15, 10411-10433, doi:10.5194/acp-15-
1077 10411-2015, 2015.

1078 Knote, C., Hodzic, A., and Jimenez, J. L.: The effect of dry and wet deposition of
1079 condensable vapors on secondary organic aerosols concentrations over the continental
1080 US, Atmos. Chem. Phys., 15, 1-18, doi:10.5194/acp-15-1-2015, 2015.

1081 Knote, C., Hodzic, A. et al.: Simulation of semi-explicit mechanisms of SOA formation
1082 from glyoxal in aerosol in a 3-D model, Atmos. Chem. Phys., 14, 6213-6239,
1083 doi:10.5194/acp-14-6213-2014, 2014.

1084 Kroll, J.H., Smith, J.D., Che, D.L., Kessler, S.H., Worsnop, D.R., and K.R. Wilson:
1085 Measurement of fragmentation and functionalization pathways in the heterogeneous
1086 oxidation of oxidized organic aerosol, Physical Chemistry Chemical Physics, 11: 8005-
1087 8014, 2009.

1088 La, Y.S., Camredon, M., Ziemann, P.J., Valorso, R., Matsunaga, A., Lannuque, V., Lee-
1089 Taylor, J., Hodzic, A., Madronich, S., Aumont B., Impact of chamber wall loss of gaseous
1090 organic compounds on secondary organic aerosol formation: explicit modeling of SOA
1091 formation from alkane and alkene oxidation, submitted ACPD, 2015.

1092 Lane, T., Donahue, N., Pandis, S., Simulating secondary organic aerosol for- mation
1093 using the volatility basis-set approach in a chemical transport model. Atmos. Environ. 42,
1094 7439e7451, 2008.

1095 Lee-Taylor, J., Madronich, S., Aumont, B., Baker, A., Camredon, M., Hodzic, A., Tyndall,
1096 G. S., Apel, E., and Zaveri, R. A.: Explicit modeling of organic chemistry and secondary
1097 organic aerosol partitioning for Mexico City and its outflow plume, Atmos. Chem. Phys.,
1098 11, 13219-13241, doi:10.5194/acp-11-13219-2011, 2011.

1099 Lelieveld, J., Evans, J.S., Fnais, M., Giannadaki, D., Pozzer, A., The contribution of
1100 outdoor air pollution sources to premature mortality on a global scale, Nature 525, 367–
1101 371, doi:10.1038/nature15371, 2015.

1102 Lim SS, Vos T, Flaxman AD, Danaei G, Shibuya K, Adair-Rohani H, et al. A comparative
1103 risk assessment of burden of disease and injury attributable to 67 risk factors and risk
1104 factor clusters in 21 regions, 1990–2010: a systematic analysis for the Global Burden of
1105 Disease Study 2010. Lancet 2012; 380(9859):2224–60. Erratum in Lancet 2013 Feb
1106 23;381(9867):628.

1107 Liu, H., Jacob, D.J., Bey, I., Yantosca, R.M., Constraints from 210Pb and 7Be on wet
1108 deposition and transport in a global three-dimensional chemical tracer model driven by
1109 assimilated meteorological fields. J. Geophys. Res. 106, 12109-12128, 2001.

1110 Madronich, S., The atmosphere and UV-B radiation at ground level. Environmental UV
1111 Photobiology, Plenum Press, 1–39, 1993.

1112 Matsunaga A., and Ziemann P.J., Gas-Wall Partitioning of Organic Compounds in a
1113 Teflon Film Chamber and Potential Effects on Reaction Product and Aerosol Yield
1114 Measurements, Aerosol Science and Technology, 44:10, 881-892, DOI:
1115 10.1080/02786826.2010.501044, 2010.

1116 Moise, T., and Rudich, Y. Reactive uptake of ozone by aerosol associated unsaturated
1117 fatty acids: Kinetics, mechanism, and products. J. Phys. Chem. A 106, 6469–6476,
1118 2002.

1119 Moise, T., R. K. Talukdar, G. J. Frost, R. W. Fox, and Y. Rudich, Reactive uptake of
1120 NO3 by liquid and frozen organics, J. Geophys. Res., 107(D2), 4014,
1121 doi:10.1029/2001JD000334, 2002.

1122 Moise, T., and Y. Rudich, Reactive uptake of ozone by proxies for organic aerosols:
1123 Surface versus bulk processes, J. Geophys. Res., 105(D11), 14667–14676,
1124 doi:10.1029/2000JD900071, 2000.

1125 Molina, M.J., Ivanov, A.V., Trakhtenberg, S. and Molina, L.T. Atmospheric evolution of
1126 organic aerosol. Geophys. Res. Lett. 31, L22104, 2004.

1127 Ortega, A. M., Hayes, P. L., Peng, Z., Palm, B. B., Hu, W., Day, D. A., Li, R., Cubison,
1128 M. J., Brune, W. H., Graus, M., Warneke, C., Gilman, J. B., Kuster, W. C., de Gouw, J.
1129 A., and Jimenez, J. L.: Real-time measurements of secondary organic aerosol formation
1130 and aging from ambient air in an oxidation flow reactor in the Los Angeles area, Atmos.
1131 Chem. Phys. Discuss., 15, 21907-21958, doi:10.5194/acpd-15-21907-2015, 2015.

1132 Pye, H. O. T. and Seinfeld, J. H.: A global perspective on aerosol from low-volatility
1133 organic compounds, Atmos. Chem. Phys., 10, 4377–4401, doi:10.5194/acp-10-4377-
1134 2010, 2010.

1135 Paulot, F., Crounse, J. D., Kjaergaard, H. G., Kuerten, A., St. Clair, J. M., Seinfeld, J. H.
1136 and Wennberg, P. O., Unexpected Epoxide Formation in the Gas-Phase Photooxidation
1137 of Isoprene. Science, 325 (5941). pp. 730-733. ISSN 0036-8075, 2009.

1138 Rienecker, M. M., Suarez, M. J., Gelaro, R., Todling, R., Bacmeister, J., Liu, E.,
1139 Bosilovich, M. G., Schubert, S. D., Takacs, L., and Kim, G.-K.: MERRA: NASA's modern-
1140 era retrospective analysis for research and applications, Journal of Climate, 24, 3624-
1141 3648, 2011.

1142 Robinson, A. L., N. M. Donahue, M. Shrivastava, E. A. Weitkamp, A. M. Sage, A. P.
1143 Grieshop, T. E. Lane, J. R. Pierce, and S. N. Pandis, Rethinking organic aerosols:
1144 Semivolatile emissions and photochemical aging, Science, 315(5816), 1259–1262,
1145 doi:10.1126/science.1133061, 2007.

1146 Seinfeld, J.H. and S.N. Pandis, Atmospheric Chemistry and Physics: From Air Pollution
1147 to Climate Change, 2nd Ed., John Wiley and Sons, Hoboken, New Jersey, 2006.

1148 Shrivastava, M., R. C. Easter, X. Liu, A. Zelenyuk, B. Singh, K. Zhang, P.-L. Ma, D.
1149 Chand, S. Ghan, J. L. Jimenez, Q. Zhang, J. Fast, P. J. Rasch, and P. Tiitta, Global
1150 transformation and fate of SOA: Implications of low-volatility SOA and gas-phase
1151 fragmentation reactions. J. Geophys. Res. Atmos., 120, 4169–4195. doi:
1152 10.1002/2014JD022563, 2015.

1153 Shrivastava, M., Fast, J., Easter, R., Gustafson Jr, W. I., Zaveri, R. A., Jimenez, J. L.,
1154 Saide, P., and Hodzic, A.: Modeling organic aerosols in a megacity: comparison of
1155 simple and complex representations of the volatility basis set approach, Atmos. Chem.
1156 Phys., 11(13), 6639-6662, doi:10.5194/acp-11-6639-2011, 2011.

1157 Simpson, D., K. E. Yttri, Z. Klimont, K. Kupiainen, A. Caseiro, A. Gelencse´r, C. Pio, H.
1158 Puxbaum, and M. Legrand, Modeling carbonaceous aerosol over Europe: Analysis of
1159 the CARBOSOL and EMEP EC/OC campaigns, J. Geophys. Res., 112, D23S14,
1160 doi:10.1029/2006JD008158, 2007.

1161 Spracklen, D.V., Jimenez, J.L., Carslaw, K.S., Worsnop, D.R., Evans, M.J., Mann, G.W.,
1162 Zhang, Q., Canagaratna, M.R., Allan, J., Coe, H., McFiggans, G., Rap, A. and Forster,
1163 P. Aerosol mass spectrometer constraint on the global secondary organic aerosol
1164 budget. Atmos. Chem. Phys. 11, 12109–12136, 2011.

1165 St. Clair, J. M., Rivera-Rios, J. C., Crounse, J. D., Knap, H. C., Bates, K. H., Teng, A. P.,
1166 Jørgensen, S., Kjaergaard, H. G., Keutsch, F. N., and Wennberg, P. O.: Kinetics and
1167 Products of the Reaction of the First-Generation Isoprene Hydroxy Hydroperoxide
1168 (ISOPOOH) with OH, J. Phys. Chem. A, doi: 10.1021/acs.jpca.5b06532, 2015.
1169 doi:10.1021/acs.jpca.5b06532, 2015.

1170 Surratt, J. D., Chan, A. W. H., Eddingsaas, N. C., Chan, M., Loza, C. L., Kwan, A. J.,
1171 Hersey, S. P., Flagan, R. C., Wennberg, P. O., and Seinfeld, J. H.: Reactive
1172 intermediates revealed in secondary organic aerosol formation from isoprene, Proc. Nat.
1173 Acad. Sci., 107, 6640-6645, doi:10.1073/pnas.0911114107, 2010.

1174 Tsigaridis, K., Daskalakis, N., Kanakidou, M., Adams, P. J., Artaxo, P., Bahadur, R.,
1175 Balkanski, Y., Bauer, S. E., Bellouin, N., Benedetti, A., Bergman, T., Berntsen, T. K.,
1176 Beukes, J. P., Bian, H., Carslaw, K. S., Chin, M., Curci, G., Diehl, T., Easter, R. C.,
1177 Ghan, S. J., Gong, S. L., Hodzic, A., Hoyle, C. R., Iversen, T., Jathar, S., Jimenez, J. L.,
1178 Kaiser, J. W., Kirkevåg, A., Koch, D., Kokkola, H., Lee, Y. H, Lin, G., Liu, X., Luo, G.,
1179 Ma, X., Mann, G. W., Mihalopoulos, N., Morcrette, J.-J., Müller, J.-F., Myhre, G.,
1180 Myriokefalitakis, S., Ng, N. L., O'Donnell, D., Penner, J. E., Pozzoli, L., Pringle, K. J.,
1181 Russell, L. M., Schulz, M., Sciare, J., Seland, Ø., Shindell, D. T., Sillman, S., Skeie, R.
1182 B., Spracklen, D., Stavrakou, T., Steenrod, S. D., Takemura, T., Tiitta, P., Tilmes, S.,
1183 Tost, H., van Noije, T., van Zyl, P. G., von Salzen, K., Yu, F., Wang, Z., Wang, Z.,
1184 Zaveri, R. A., Zhang, H., Zhang, K., Zhang, Q., and Zhang, X.: The AeroCom evaluation
1185 and intercomparison of organic aerosol in global models, Atmos. Chem. Phys., 14,
1186 10845-10895, doi:10.5194/acp-14-10845-2014, 2014.

1187 Tsimpidi, A. P., V. A. Karydis, M. Zavala, W. Lei, L. Molina, I. M. Ulbrich, J. L. Jimenez,
1188 and S. N. Pandis, Evaluation of the volatility basis-set approach for the simulation of
1189 organic aerosol formation in the Mexico City metropolitan area, Atmos. Chem. Phys.,
1190 10(2), 525-546, 2010.

1191 Wesely, M.L., Parameterizations of surface resistance to gaseous dry deposition in
1192 regional-scale, numerical models. Atmos. Environ. 23, 1293–1304, 1989.

1193 Wiscombe, W.J., Improved Mie scattering algorithms. Appl. Opt. 19, 1505-1509, 1980.

1194 Wong, J.P.S, Zhou, S., and Abbatt, P.D.: Changes in Secondary Organic Aerosol
1195 Composition and Mass due to Photolysis: Relative Humidity Dependence. J. Phys.
1196 Chem. A, Article ASAP, DOI: 10.1021/jp506898c, 2014.

1197 Zhang, X., Cappa, C. D., Jathar, S. H., McVay, R. C., Ensberg, J. J., Kleeman, M. J.,
1198 and Seinfeld, J. H.: Influence of vapor wall loss in laboratory chambers on yields of
1199 secondary organic aerosol, P. Natl. Acad. Sci. USA, 111, 5802–5807, 2014.

1200 Zhang, Q., Jimenez, J. L., Canagaratna, M. R., Allan, J. D., Coe, H., Ulbrich, I., et al.:
1201 Ubiquity and dominance of oxygenated species in organic aerosols in anthropogenically-
1202 influenced Northern Hemisphere midlatitudes, Geophysical Research Letters, 34, 6,
1203 L13801, 10.1029/2007gl029979, 2007.

1204 Yttri, K., Aas, W., Bjerke, A., Ceburnis, D., Dye, C., Emblico, L., Facchini, M., Forster, C.,
1205 Hanssen, J., Hansson, H.. Elemental and organic carbon in PM10: a one year
1206 measurement campaign within the European Monitoring and Evaluation Programme
1207 EMEP. Atmos. Chem. Phys., 7, 5711-5725, doi:10.5194/acp-7-5711-2007, 2007.

1208

Table 1: Parameters used in the new volatility basis set (VBS_NEW). Wall corrected mass yields are based on the Statistical Oxidation Model (SOM) fit to the chamber data from *Zhang et al.* [2014]. For isoprene, an isoprene-specific version of SOM was used (see Supplementary Material for details). IVOC yields are derived from the explicit model GECKO-A simulations performed for n-alkanes mixtures at low (0.1 ppb) and high (10 ppb) NO_X levels. For SOM and GECKO-A fits, yields were derived assuming background OA concentrations of 10 µg m^{-3}.

Precursor	**IVOC**	**TERP**	**ISOP**	**BENZ**	**TOL**	**XYL**	**SESQ**
Mw g mol^{-1}	189	136	68	78	92	106	204
$k_{OH@298K}$ (s^{-1})	1.34×10^{-11}	5.3×10^{-11}	10^{-10}	1.22×10^{-12}	5.63×10^{-12}	2.31×10^{-11}	5.3×10^{-11}
Log[C*]	Mass yields at low NO_X						
< -2	0.315	0.093	0.012	0.007	0.371	0.395	0.270
-1	0.173	0.211	0.013	0.003	0.028	0.041	0.253
0	0.046	0.064	0.001	0.270	0.207	0.203	0.080
1	0.010	0.102	0.100	0.142	0.586	0.121	0.157
2	0.007	0.110	0.078	0.400	0.063	0.232	0.068
3	0.008	0.125	0.097	0.120	0.138	0.145	0.072
	Mass yields at high NO_X						
< -2	0.140	0.045	0.001	0.031	0.042	0.015	0.157
-1	0.136	0.015	0.001	0.011	0.123	0.056	0.220
0	0.069	0.142	0.027	0.507	0.263	0.006	0.083
1	0.019	0.061	0.021	0.019	0.020	0.026	0.097
2	0.010	0.074	0.044	0.030	0.319	0.087	0.054
3	0.012	0.165	0.185	0142	0.329	0.193	0.100

Table 2: Henry's law constants used in this study based on values reported in *Hodzic et al.* [2014]. H^{eff} of the oxidation products of n-alkanes is used for oxidation products of all anthropogenic precursors whereas H^{eff} of the oxidation products of monoterpenes is used for those of biogenics. For products of IVOCs used in table 1, we use $H^{eff} = 10^3$ M atm^{-1}.

Saturation concentrations (µg m^{-3})	0.01	0.1	1	10	100	1000
Anthropogenic: H^{eff} n-alkanes (M atm^{-1})	1.3×10^{7}	3.2×10^{5}	4.0×10^{5}	1.3×10^{5}	1.6×10^{5}	10^{5}
Biogenic: H^{eff} monoterpenes (M atm^{-1})	7.9×10^{11}	6.3×10^{10}	3.2×10^{9}	6.3×10^{8}	3.2×10^{7}	1.3×10^{7}

1221 Table 3: Chemical speciation of the considered SVOC and IVOC mixtures in GECKO-A
1222 [*Lee-Taylor et al.*, 2011].

Surrogate	species	Nb. C	Contribution to surrogate
IVOC	n-dodecane	12	22.50%
	n-tridecane	13	20.80%
	n-tetradecane	14	15.70%
	n-pentadecane	15	11.30%
	n-hexadecane	16	10.60%
	n-heptadecane	17	8.00%
	n-octadecane	18	7.50%
	n-nonadecane	19	3.60%
SVOC	n-nonadecane	19	9.10%
	n-eicosane	20	17.40%
	n-henicosane	21	16.60%
	n-docosane	22	9.50%
	n-tricosane	23	9.10%
	n-tetracosane	24	7.70%
	n-pentacosane	25	6.50%
	n-hexacosane	26	6.20%
	n-heptacosane	27	3.90%
	n-octacosane	28	3.70%
	n-nonacosane	29	3.00%
	n-triacontane	30	7.30%

1223

1224 Table 4: Description of the GEOS-Chem simulations performed for years 2004-2008.

Simulation	**Production**	***Heff* (M atm^{-1}) for dry and wet deposition**	**SOA photolysis**	**SOA+ O_3**
REF	VBS_REF [*Jo et al.*, 2013]	10^5	NO	NO
NY	VBS_NEW (Table 1)	10^5	NO	NO
NY_D	VBS_NEW (Table 1)	Volatility dependent $H^{eff(*)}$	NO	NO
NY_DP	VBS_NEW (Table 1)	Volatility dependent H^{eff} $^{(*)}$	$4\times10^{-4}\times J_{NO2}{}^{(**)}$	NO
NY_DPH	VBS_NEW (Table 1)	Volatility dependent H^{eff} $^{(*)}$	$4\times10^{-4}\times J_{NO2}{}^{(**)}$	YES

1225 $^{(*)}$ based on the H^{eff} parameterization by *Hodzic et al.* [2014]; $^{(**)}$ from *Hodzic et al.* [2015].

Table 5: Global annual average budgets for organic gases and particles for the 4 year (2005-2008) period. VOC from anthropogenic, biomass burning (BB) and biogenic sources are indicated, as well as S/IVOC from anthropogenic and BB sources.

Sources of oxygenated species	Gas Production (Tg yr^{-1})	Gas Burden (Tg)	Gas Dry Deposition (Tg yr^{-1})	Gas Wet Deposition (Tg yr^{-1})	Net particle production[1] (Tg yr^{-1})	Particle Dry Dep. (Tg yr^{-1})	Particle Wet Dep. (Tg yr^{-1})	Photolytic/heterogeneous loss (Tg yr^{-1})	Particle Burden (Tg)	Particle lifetime (days)
REF run										
Anthro. and BB VOC	21.1	0.04	3.0	3.4	14.7	1.9	12.8	0	0.35	8.6
Biogenic VOC	151.5	1.03	48.6	84.6	21.5	2.2	19.3	0	0.53	9.0
Total[1]	172.6	1.07	51.6	88.0	36.2	4.1	32.1	0	0.88	
Primary					Source: 56.4	9.9	46.5	0	0.94	6.1
NY run										
Anthro. and BB VOC	16.0	0.1	3.5	5.0	7.4	0.95	6.5	0	0.20	10
Biogenic VOC	228.1	1.1	44.9	83.9	99.3	9.4	89.9	0	1.62	6
Anthro. and BB I/SVOC	27.7	0.02	1.1	1.4	25.2	3.15	22.1	0	0.48	7
Total[1]	271.8	1.2	49.5	90.4	132	13.5	118.5	0	2.31	
Primary					Source: 56.4	9.9	46.5	0	0.94	6.1
NY_DPH run										
Anthro. and BB VOC	16.0	0.07	3.0	4.3	8.8	0.6	3.8	4.3	0.08	3.3
Biogenic VOC	228.1	0.617	71.8	58.8	97.5	6.3	56.5	34.7	0.59	2.2
Anthro. and BB I/SVOC	27.7	0.014	0.7	1.0	25.9	2.0	12.6	11.3	0.21	3.0
Total[2]	271.8	0.701	75.5	64.1	132.2	8.9	73.0	50.3	0.88	

[1]: Net particle production included the condensation and evaporation of organic gases.

[2]: "Total" refers to the total SOA including ASOA, BSOA and when available IS-SOA.

1234 Table 6: Global annual-average lifetimes for organic gases and particles for the 4 year
1235 (2005-2008) period. VOC from anthropogenic, biomass burning (BB) and biogenic
1236 sources are indicated, as well as S/IVOC from anthropogenic and BB sources.

Sources of oxygenated species	Gas Dry Deposition Lifetime (days)	Gas Wet Depostion Lifetime (days)	Particle Dry Deposition Lifetime (days)	Particle Wet Deposition Lifetime (days)	Particle Chem Loss Lifetime (days)	Particle Overall Lifetime (days)
REF SIMULATION						
Anthro. and BB VOC	5.0	4.4	66.5	9.9	NA	8.6
Biogenic VOC	7.7	4.4	87.4	10.1	NA	9.0
NY SIMULATION						
Anthro. and BB VOC	9.4	6.8	78.2	11.5	NA	10.0
Biogenic VOC	8.7	4.7	63.1	6.6	NA	6.0
Anthro. and BB I/SVOC	7.2	5.4	55.7	8.0	NA	7.0
NY_DPH SIMULATION						
Anthro. and BB VOC	8.5	6.1	43.3	7.4	6.6	3.3
Biogenic VOC	3.1	3.8	34.4	3.8	6.2	2.2
Anthro. and BB I/SVOC	6.8	5.1	38.4	6.1	6.8	3.0

1237

1238

1239

Figures:

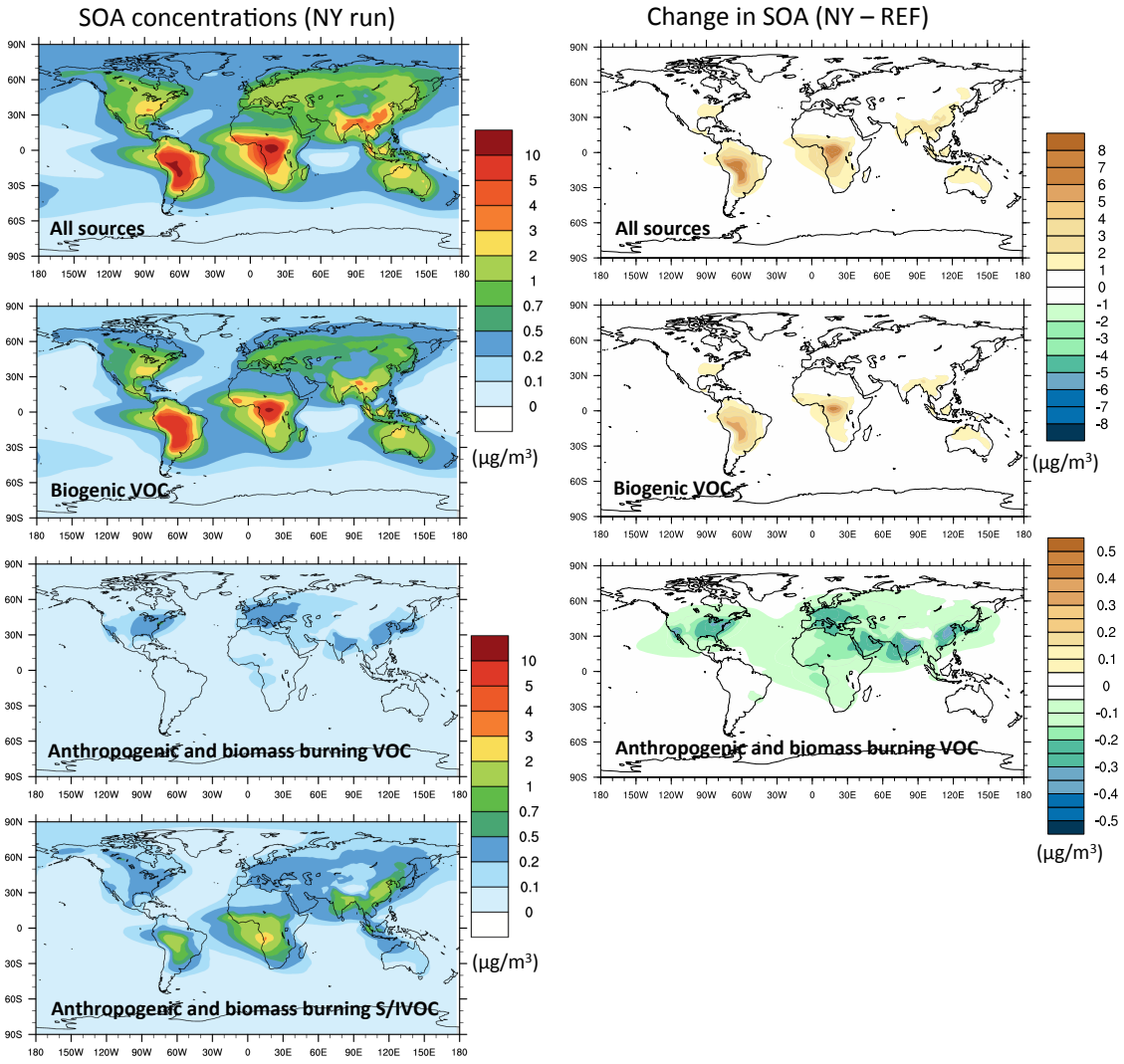

Figure 1: 2005-2008 average concentrations for SOA and its constituents as predicted by the GEOS-Chem NY run in the lower troposphere (surface to 5km; left column). Total SOA is separated into SOA from biogenic VOCs, anthropogenic and biomass burning traditional VOCs, and anthropogenic and biomass burning I/SVOC. The NY run is also compared with REF (right column).

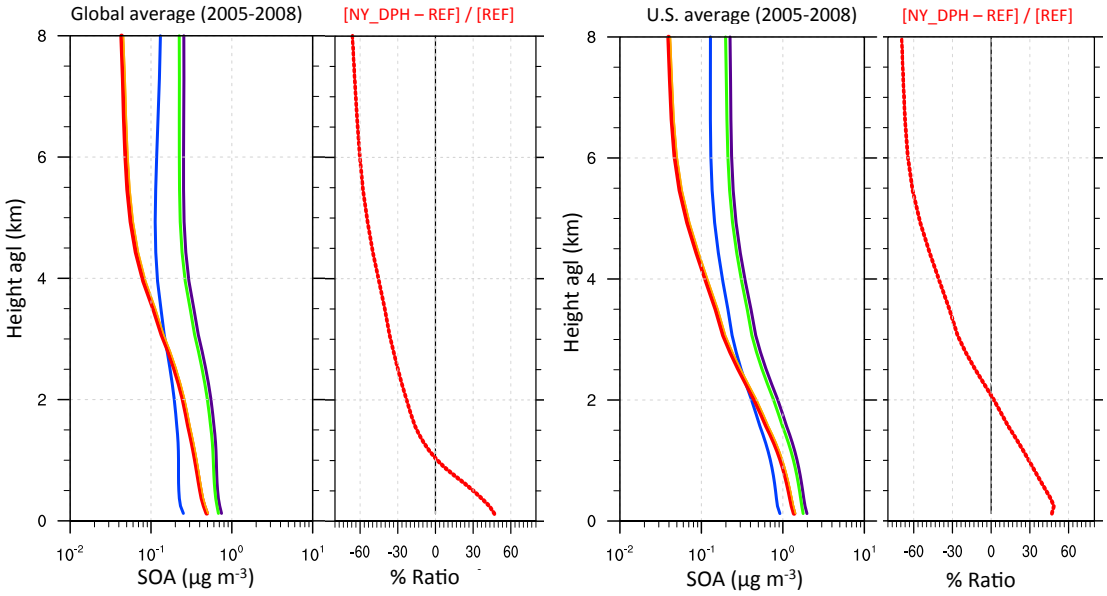

Figure 2: Vertical profiles of average SOA concentrations (at ambient temperature and pressure) integrated globally and regionally over the continental U.S. between 2005 and 2008. The ratios between SOA predictions by the NY_DPH and REF runs are also shown for each region.

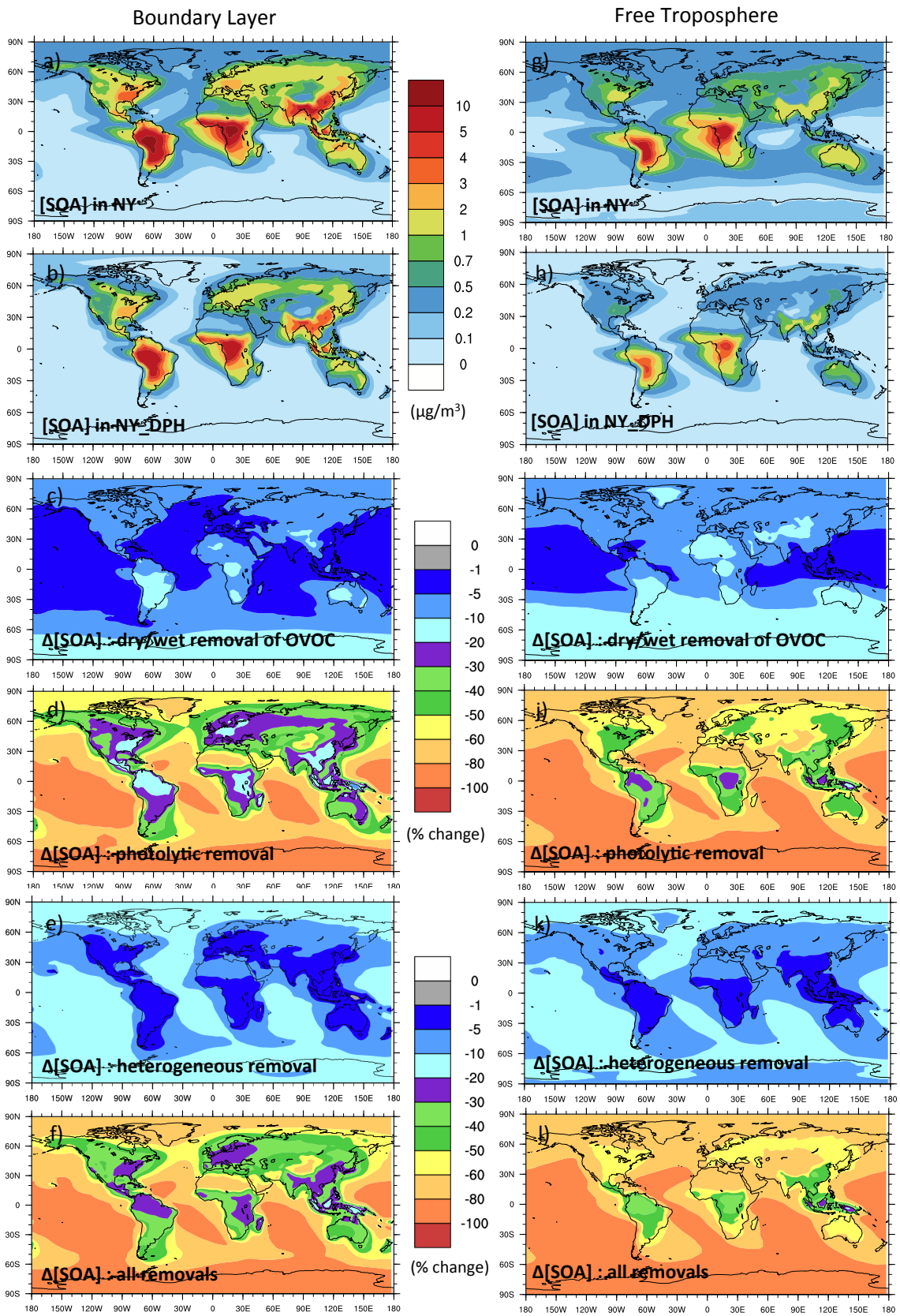
Boundary Layer
Free Troposphere
a)
[SOA] in NY
g)
[SOA] in NY
b)
[SOA] in NY_DPH
h)
[SOA] in NY_DPH
10
5
4
3
2
1
0.7
0.5
0.2
0.1
0
(μg/m3)
c)
Δ[SOA] : dry/wet removal of OVOC
i)
Δ[SOA] : dry/wet removal of OVOC
d)
Δ[SOA] : photolytic removal
j)
Δ[SOA] : photolytic removal
0
-1
-5
-10
-20
-30
-40
-50
-60
-80
-100
(% change)
e)
Δ[SOA] : heterogeneous removal
k)
Δ[SOA] : heterogeneous removal
f)
Δ[SOA] : all removals
l)
Δ[SOA] : all removals
(% change)

1312

Figure 3: Average SOA concentrations for 2005-2008 as predicted by NY and NY_DPH runs in the boundary layer (surface to 1.5km; left column) and in the free troposphere (1.5-5km; right column). Percent decrease in SOA concentrations resulting from dry/wet removal ([NY_D - NY] / [NY]), photolytic removal ([NY_DP – NY_D] / [NY_D]) and heterogeneous removal ([NY_DPH – NY_DP] / [NY_DP]) of SOA. The combined effect of all considered removal pathways on SOA concentrations is also shown ([NY_DPH - NY] / [NY]).

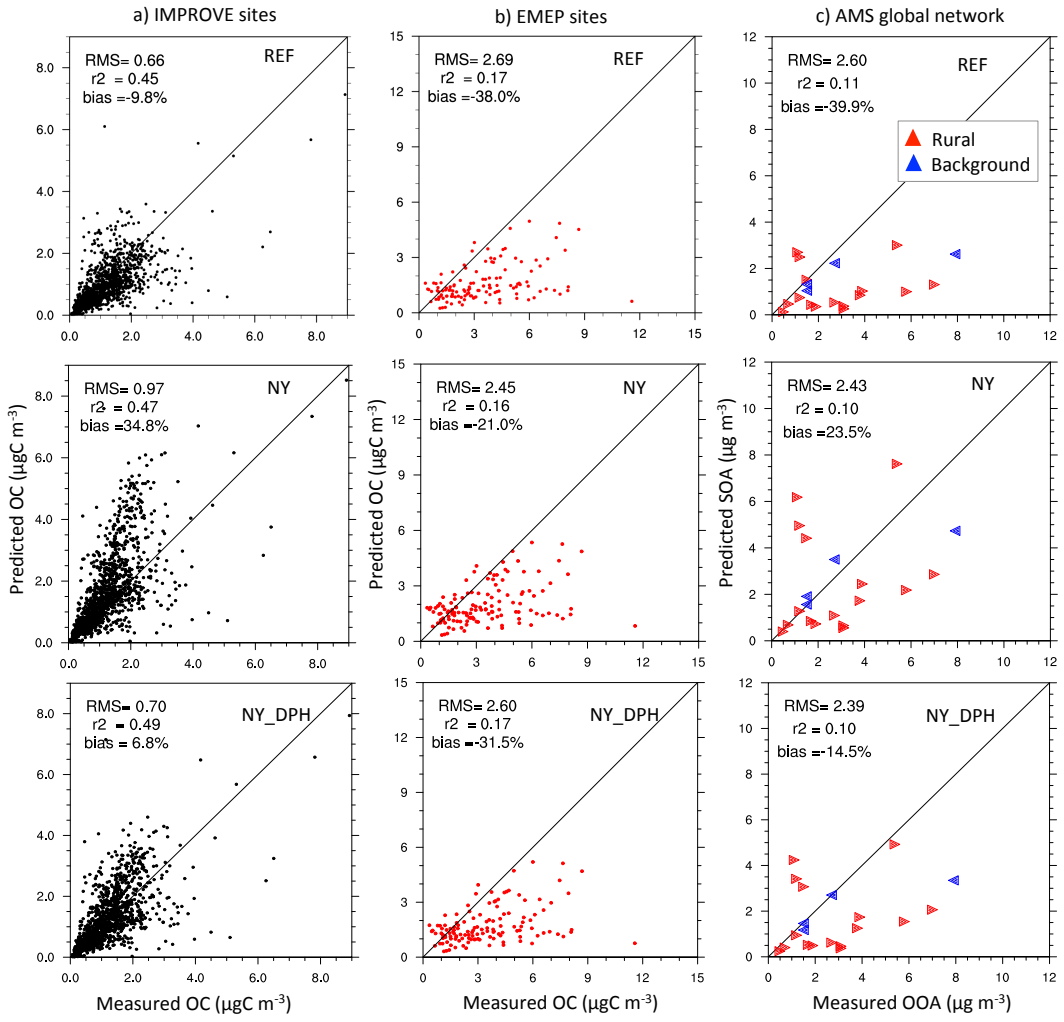

Figure 4: Scatter plots of predicted vs. measured monthly mean OC (µgC m^{-3}) and SOA (µg m^{-3}) at the surface sites of the U.S. IMPROVE network, the European EMEP network and the global AMS network. AMS data are divided into rural sites (red) and background sites (blue). Given model coarse horizontal resolution, urban sites were not considered. Modeled monthly mean values are representative of years 2005 to 2008 and are

compared with monthly mean observations averaged over 2005-2008 for IMPROVE, and 2002-2003 for EMEP sites.

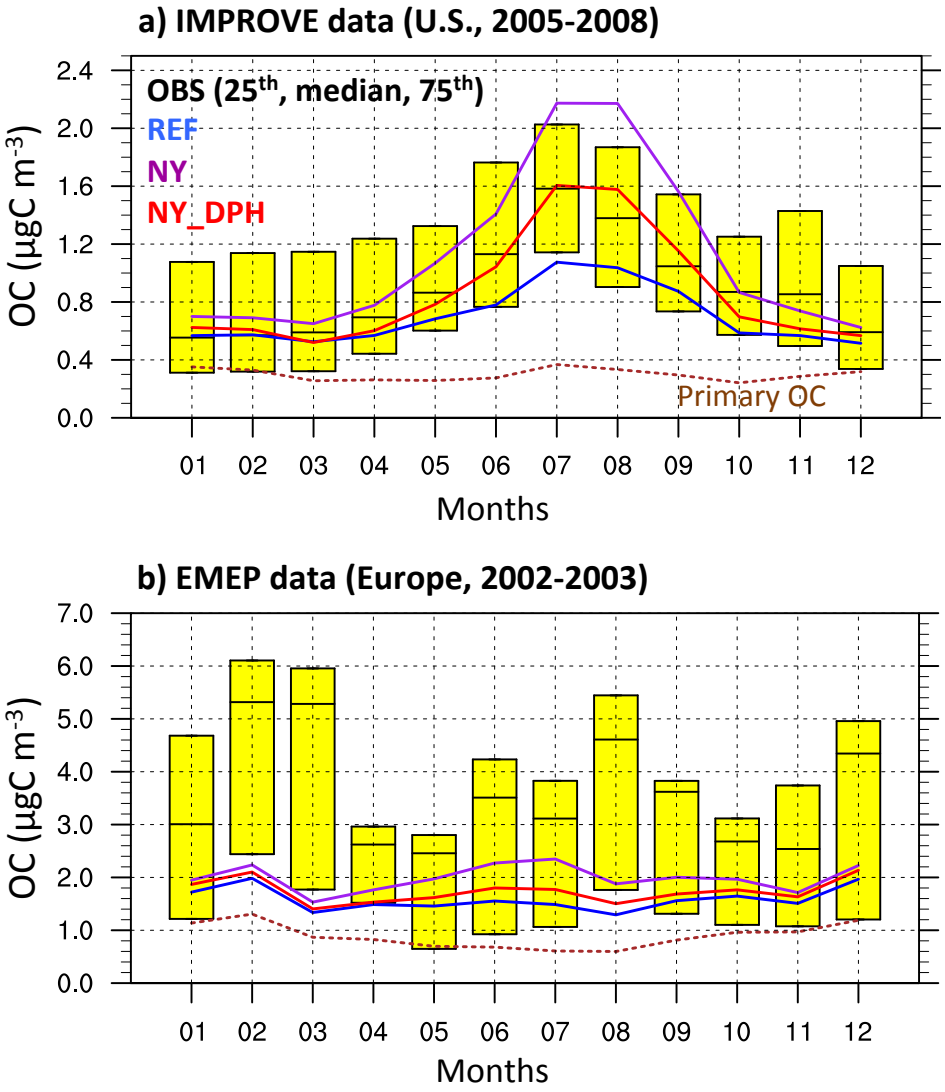

Figure 5: Monthly average OC concentrations as predicted by the GEOS-Chem 2005-2008 simulations, and as measured by (a) the IMPROVE network (2005-2008) and (b) the EMEP network (2002-2003). The yellow boxes show the observed medians, 25th and 75th quintiles reflecting the spatial (among stations) and temporal (among years) variability. The predicted OC medians are shown for the REF (blue), NY (purple) and NY_DPH (red) simulations. The predicted primary OC is also shown (brown dashed line) and is similar for all simulations.

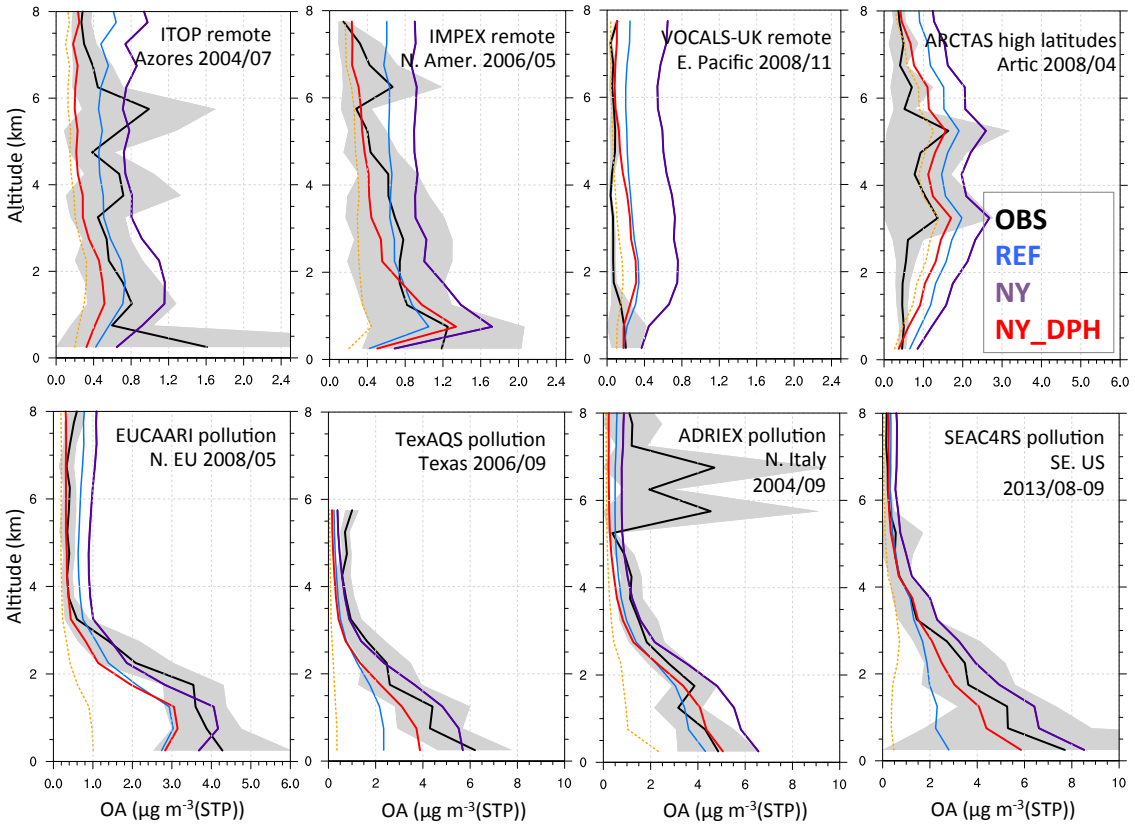

Figure 6: Comparison of mean OA vertical profiles (µg m^{-3}(STP) at 288.15K and 1013.25 hPa) measured during recent aircraft field campaigns (see Table S5) with the corresponding GEOS-Chem predictions from 3 simulations including REF (blue), NY (green) and NY_DPH (red). Concentrations of primary OC are also shown (dashed red line) and are similar in all model runs. Flights in remote or high latitude (top row), and moderately polluted (bottom row) regions are shown. Variability around observed values (2 standard deviations) at each altitude are shown with shaded area. For ARCTAS, the observed OA concentrations above the 99th percentile i.e. larger than 16 µg m^{-3}(STP were filtered out to limit the influence of biomass burning plumes. For SEAC4RS the observations of acetonitrile were used to filter out fire plumes, and data above the 80th percentile (~140ppt) of observed acetonitrile concentrations were excluded. The model simulations are sampled for the year, month and locations of each aircraft campaign except for two campaigns including ITOP and ADRIEX for which average values between 2005-2008 are used for the month matching the field project.

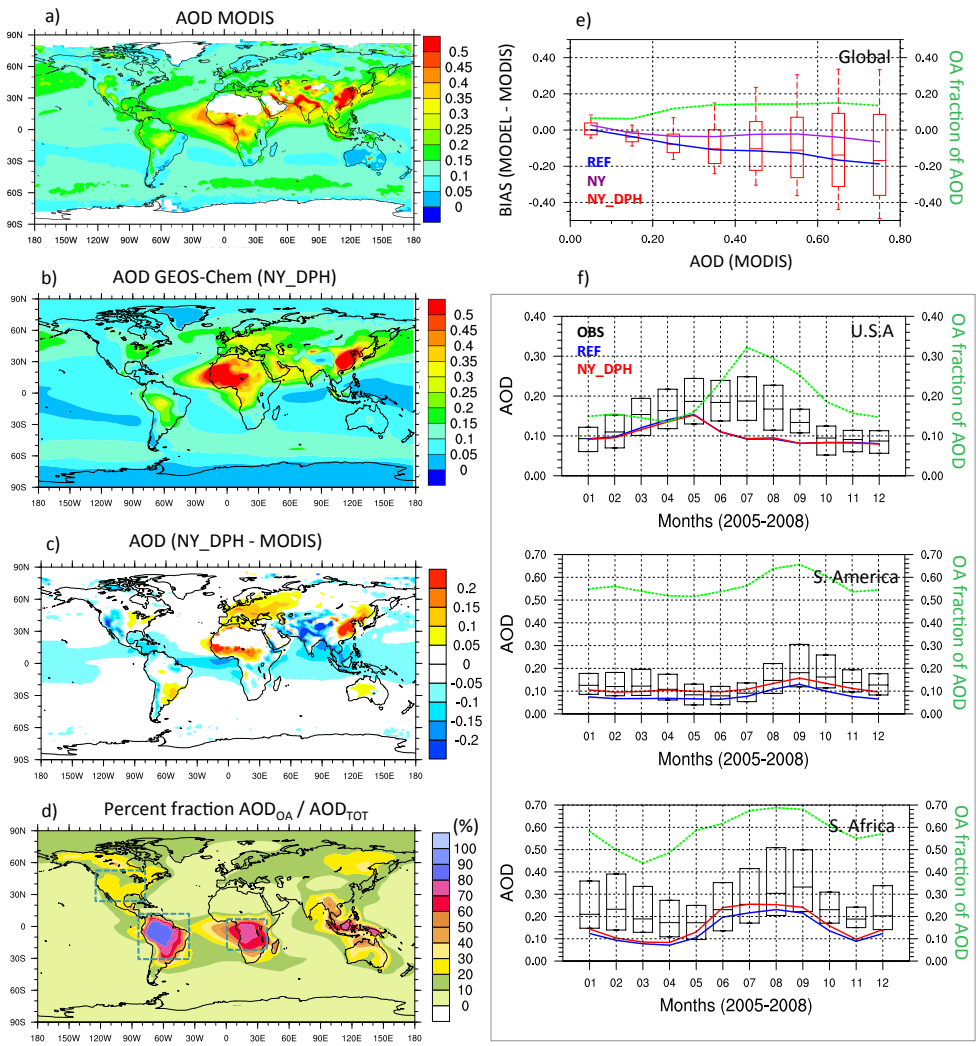

Figure 7: Comparison of 2005-2008 averaged AOD levels as measured by MODIS (Aqua and Terra) and predicted by the GEOS-Chem NY_DPH simulation. The difference (c) between modeled and observed AODs is also shown, only for days/locations when observations are available. The dependence of the model bias on the AOD levels is also shown (e). (d) shows the contribution of organic aerosols to total modeled AOD for the NY_DPH simulations, which allows to identify regions where AOD predictions are highly sensitive to SOA predictions. (f) shows the predicted and observed 2005-2008 monthly average AOD in various regions shown in (d). The boxes show the observed medians, 25th and 75th quintiles reflecting the spatial (among grid boxes in the region) and temporal (among years) variability.

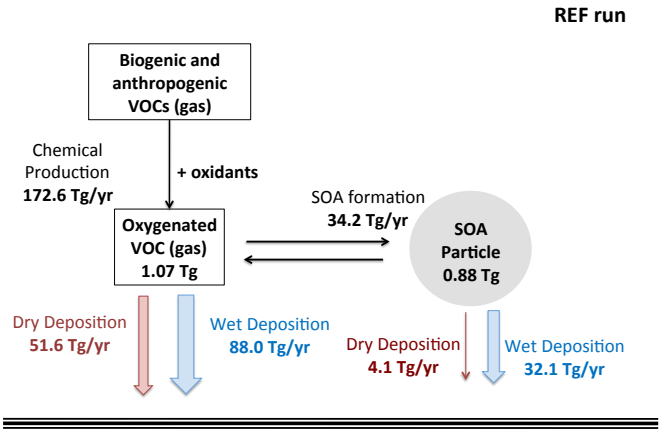

1363

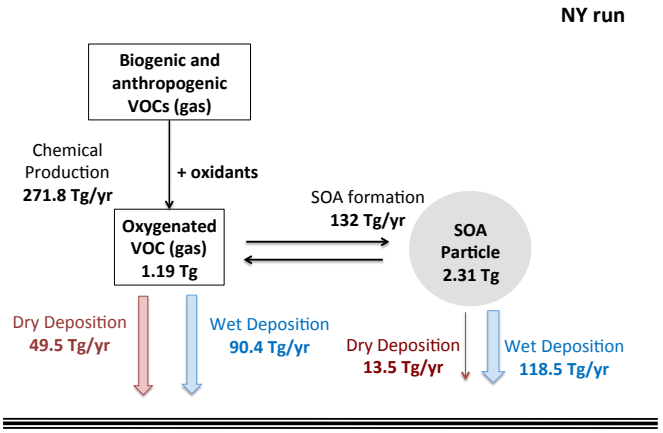

1364

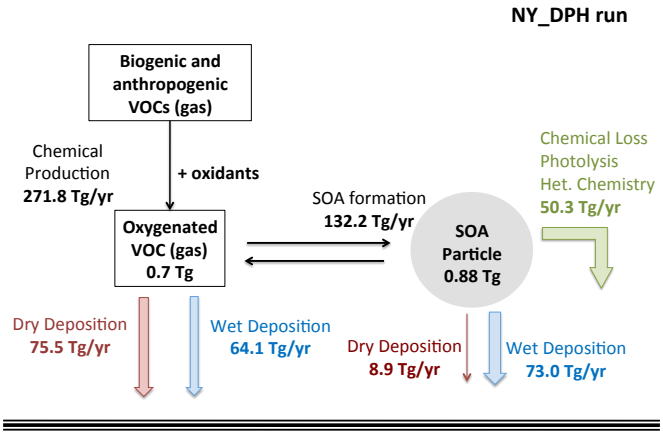

1365

1366 Figure 8: Global budgets (sources/sinks Tg yr^{-1} and burden Tg) of condensable
1367 secondary organic gas and particle compounds as predicted by the GEOS-Chem REF,
1368 NY and NY_DPH simulations for 2005-2008.

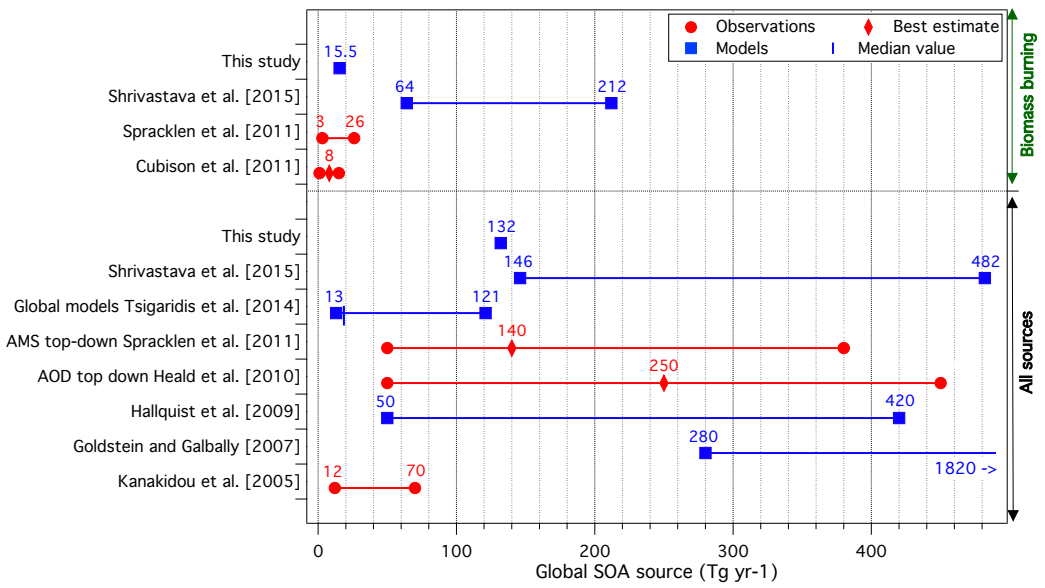

1369

1370 Figure 9: Global SOA particle-phase source (Tg yr^{-1}) as predicted in this study
1371 (NY_DPH) and as reported by previous studies. SOA production from all sources
1372 (anthropogenic, biomass burning, biofuel and biogenic) as well as from biomass burning
1373 alone is shown.

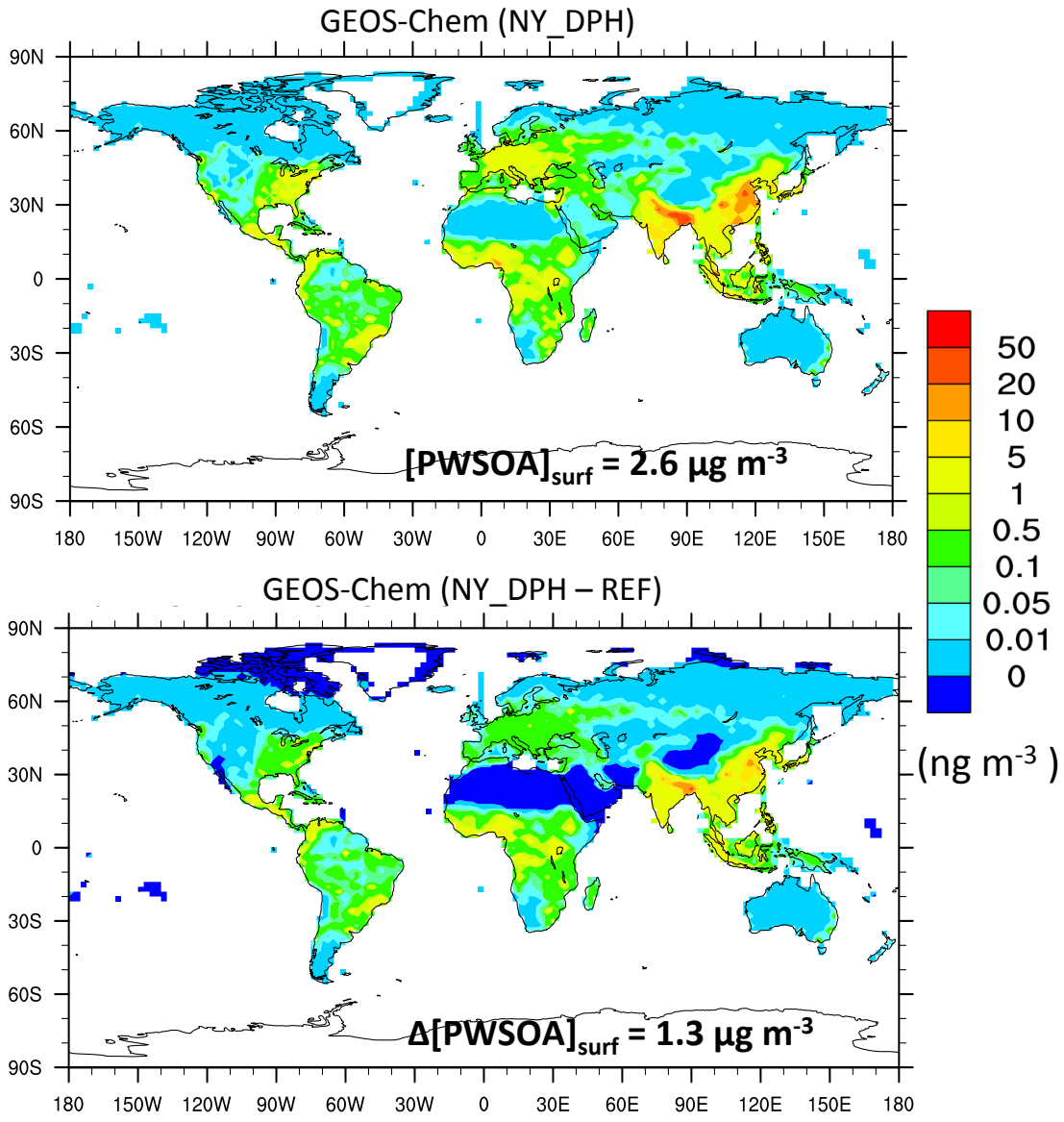

Figure 10: Contribution of individual models grid cells to global population-weighted surface SOA concentration $[PWSOA]_{surf}$ in the NY_DPH simulation (top) and to changes in in $[PWSOA]_{surf}$ between the NY_DPH and REF simulation. The total PWSOA is obtained by summing up the individual grid cell contributions shown in the figure.

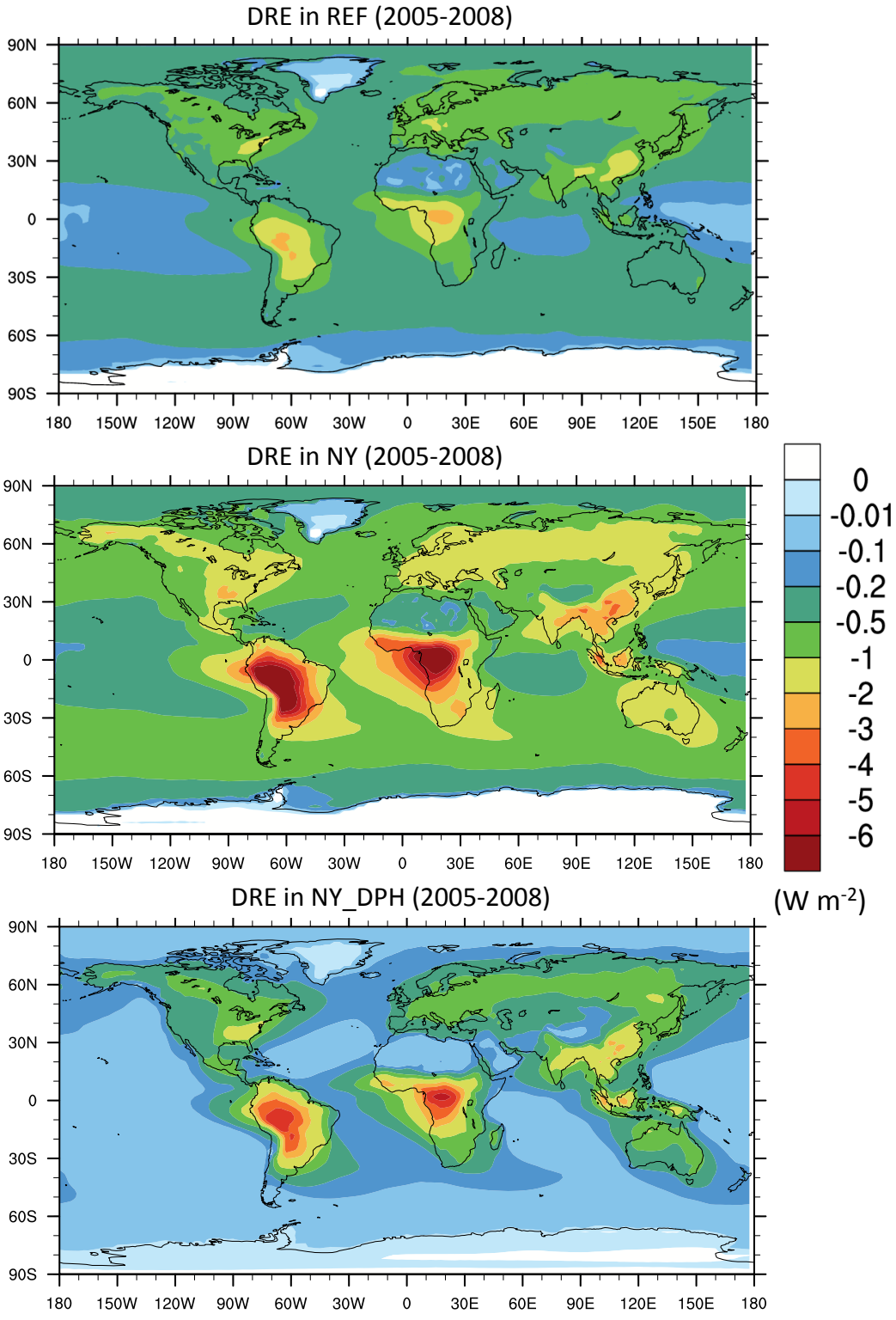

Figure 11: Simulated clear-sky SOA direct radiative effect (DRE) at the top of the atmosphere for the REF (upper), NY (middle) and NY_DPH runs (bottom).